

Infinite projected entangled-pair state methods for variational ground state simulations using automatic differentiation

Jan Naumann^{1,†,★}, Erik Lennart Weerda^{2,‡,★}, Matteo Rizzi^{2,3}, Jens Eisert^{1,4} and Philipp Scholl^{1,◦},

1 Dahlem Center for Complex Quantum Systems and Institut für Theoretische Physik, Freie Universität Berlin, Arnimallee 14, 14195 Berlin, Germany

2 Institute for Theoretical Physics, University of Cologne, 50937 Köln, Germany

3 Forschungszentrum Jülich GmbH, Institute of Quantum Control, Peter Grünberg Institut (PGI-8), 52425 Jülich, Germany

4 Helmholtz-Zentrum Berlin für Materialien und Energie, Hahn-Meitner-Platz 1, 14109 Berlin, Germany

★ Both first authors have contributed equally.

† j.naumann@fu-berlin.de,

‡ weerda@thp.uni-koeln.de,

◦ philipp.scholl@fu-berlin.de

Abstract

Tensor networks capture large classes of ground states of phases of quantum matter faithfully and efficiently. Their manipulation and contraction has remained a challenge over the years, however. For most of the history, ground state simulations of two-dimensional quantum lattice systems using (infinite) projected entangled pair states have relied on what is called a time-evolving block decimation. In recent years, multiple proposals for the variational optimization of the quantum state have been put forward, overcoming accuracy and convergence problems of previously known methods. The incorporation of automatic differentiation in tensor networks algorithms has ultimately enabled a new, flexible way for variational simulation of ground states and excited states. In this work we review the state-of-the-art of the variational iPEPS framework, providing a detailed introduction to automatic differentiation, a description of a general foundation into which various two-dimensional lattices can be conveniently incorporated, and demonstrative benchmarking results.

Copyright attribution to authors.

This work is a submission to SciPost Physics Lecture Notes.

License information to appear upon publication.

Publication information to appear upon publication.

Received Date

Accepted Date

Published Date

1

2 Contents

3	1 Introduction	3
4	2 Variational iPEPS	4
5	2.1 iPEPS setup	5
6	2.2 CTMRG backbone	6
7	2.2.1 Absorption of iPEPS tensors	8

8	2.2.2	Calculation of projectors	9
9	2.2.3	Convergence and CTMRG fixed-points	11
10	2.3	Energy expectation values	12
11	2.4	Automatic differentiation	13
12	2.5	Calculation of the gradient at the CTMRG fixed-point	15
13	2.6	Optimization	17
14	2.7	Handling of physical symmetries	18
15	2.8	Pitfalls and practical hints	18
16	2.8.1	Iterative SVD algorithm	18
17	2.8.2	Stability of the CTMRG routine	19
18	2.8.3	Prevention of local minima	20
19	2.8.4	Recycling of environments	20
20	2.8.5	Analysing iPEPS data at finite bond dimensions	20
21	2.8.6	Degenerate singular values	20
22	3	Extension to other lattices	21
23	3.1	Honeycomb lattice	21
24	3.2	Kagome lattice	22
25	3.3	Square-Kagome lattice	24
26	3.4	Triangular lattice	25
27	3.5	Comments about different structures	26
28	4	Benchmarks and discussions	27
29	4.1	Comments on lower bounds in variational principles	28
30	4.2	Honeycomb lattice	28
31	4.3	Kagome lattice	29
32	4.4	Square-Kagome lattice	30
33	4.5	Triangular lattice	31
34	4.6	Comments on excited states	32
35	4.7	Comments on fermionic systems	33
36	5	Conclusion and prospects	33
37	5.1	CO ₂ -emissions table	34
38	Appendix: Background on automatic differentiation		36
39	A	Adjoint functions and variables	36
40	B	Automatic differentiation for complex variables	37
41	C	The implicit function theorem and its use at the CTMRG fixed-point	37
42	D	Automatic differentiation in the language of differential geometry	37
43	References		41
44	<hr/>		

1 Introduction

Tensor networks are at the basis of a wealth of methods that are able to efficiently capture systems with many degrees of freedom, primarily in the context of interacting quantum systems, but also in a wide range of other fields. They have a long history: The beginnings can be seen [1] as originating from work on transfer matrices [2] for two-dimensional classical Ising models and methods of corner transfer matrices again in the context of classical spin models [3]. In more recent times, the rise of tensor networks to describe interacting quantum many-body systems can be traced back to at least two strands of research. On the one hand, the now famous *density matrix renormalization group* (DMRG) approach [4, 5] can be regarded as a variational principle over *matrix product states* [6–8], a particularly common class of one-dimensional tensor network states. What are called *finitely-correlated states* [9] have later been understood as a Heisenberg picture variant of essentially the same family of states. These families of quantum states could further be interpreted as basically parametrizing gapped phases of matter in one spatial dimension. In a separate development, *tensor trains* became a useful tool in numerical mathematics [10]. These strands of research had been developing independently for quite a while before being unified in a common language of *tensor networks* (TN) as it stands now as a pillar of research on numerical and mathematical quantum many-body physics [11–15].

Two-dimensional tensor networks, now known as *projected entangled pair states* [16], again have a long history. The intuition why they provide a good ansatz class for describing ground states of gapped quantum many-body Hamiltonians [17, 18] – as well as other families of states – is the same as for matrix product states: Such states are expected to be part of what is called the “*physical corner*” of the Hilbert space. These states feature local entanglement compared to the degrees of entanglement unstructured states would exhibit. Ground states of gapped phases of matter are thought to satisfy *area laws for the entanglement entropy* [15]. Even though some of the rigorous underpinning of this mindset is less developed in two spatial dimensions compared to the situation in one spatial dimension, there is solid evidence that projected entangled pair states provide an extraordinarily good and powerful ansatz class for meaningful states of two-dimensional quantum systems.

There is a new challenge arising in such two-dimensional tensor networks. In contrast to matrix product states, they cannot be exactly efficiently *contracted*: On general grounds, there are complexity theoretic obstructions against the efficient contraction of projected entangled pair states in worst case [19] – and even in average case [20] – complexity. The burden can be lessened by acknowledging that projected entangled pair states can be contracted in quasi-polynomial time [21]. These more conceptual insights constitute an underpinning of a quite practically minded question: This shows that to develop ways of efficiently and feasibly approximating tensor network contractions in two spatial dimensions is at the heart of the method development in the field.

Consequently, over the years, several numerical methods of approximately contracting projected entangled pair states have been developed. In fact, much of the method development has been along these lines. In the focus of attention in this work are projected entangled pair states directly in the thermodynamic limit, commonly referred to as *infinite projected entangled pair states* (iPEPS) [22–24]. The contraction necessary to compute expectation values of local observables gives rise to the challenge of approximately calculating effective environments. Over the years, several methods have been introduced and pursued, including methods based on boundary matrix product states [22], corner transfer matrix methods [24–26] – particularly important for the method development presented here – and tensor coarse-graining techniques [27–30].

Variational optimization algorithms for uniform matrix product states have been developed

94 that combine density matrix renormalization group methods with matrix product state tangent
 95 space concepts to find ground states of one dimensional quantum lattices in the thermody-
 96 namic limit [31, 32], building on earlier steps of devising geometrically motivated variational
 97 principles for tensor network states [33, 34]. The pursuit of such variational optimization has
 98 been particularly fruitful in the two dimensional case of iPEPS. Initially proposed methods
 99 constructed the gradient of the energy explicitly using specialized environments [35, 36].

100 Recently, as an element of major method development, the programming technique called
 101 *automatic differentiation*, widely used in the machine learning community, has been utilized for
 102 the task of calculating the gradient [37] in tensor network optimization. This step drastically
 103 simplifies the programming involved and allows one to use variational ground state search on,
 104 e.g., more exotic lattice geometries with little additional effort. Such variational approaches
 105 for iPEPS constitute the basis for this work. Automatic differentiation has also been employed
 106 in further fashions in the tensor network context in several works recently [38–41, 41–49],
 107 some of which are accompanied by publicly available code libraries [50–53]. Notably, even for
 108 gapped local Hamiltonians with chiral topological ground states, for which the numerical appli-
 109 cability of PEPS was unclear due to no-go theorems in related cases [54], the use of variational
 110 optimization has proven successful [41, 49, 55]. As a novel programming paradigm, automatic
 111 differentiation composes parameterized algorithmic components in such a way that the pro-
 112 gram becomes differentiable and its components can be optimized using gradient search. It is
 113 a sophisticated way to evaluate the derivative of a function specified by a computer program,
 114 specifically by applying the chain rule to elementary arithmetic operations. Again, it has only
 115 recently been appreciated how extremely powerful such tools are in the study of interacting
 116 quantum matter by means of tensor networks.

117 In this review article, we elaborate on these developments and comprehensively present
 118 ideas for a variational iPEPS method based on automatic differentiation. This includes a de-
 119 tailed description of the methodology and practical insights for implementations, complement-
 120 ing and extending the existing body of literature. We further introduce a versatile framework,
 121 that allows arbitrary unit cells and different two-dimensional lattices to be treated on a com-
 122 mon footing. At the same time, this work accompanies the publicly available numerical library
 123 *variPEPS* – a versatile tensor network library for variational ground state simulations in two
 124 spatial dimensions – which implements the methods described in this review [56–58].

125 The content of this work is organised in three main sections. In Sec. 2, we describe the
 126 central methods that are being used in the variational iPEPS framework as well as practical
 127 remarks regarding implementation. Furthermore, we explain in detail the basics of automatic
 128 differentiation and its application in state-of-the-art ground-state search. In Sec. 3, we then
 129 turn to explaining how to conveniently map generic lattice structures to a square one, over
 130 which the variational iPEPS methods naturally operate. Following up on this, in Sec. 4, we
 131 present numerical benchmarks obtained with the methods outlined in the previous sections
 132 and implemented in the *variPEPS* library, in comparison to other customary methods like exact
 133 diagonalization, iPEPS imaginary-time evolution and variational Monte Carlo methods.

134 2 Variational iPEPS

135 We seek to find the the TN representation of the state vector $|\psi\rangle_{\text{TN}}$ that best approximates the
 136 true ground state vector $|\psi_0\rangle$ of an Hamilton operator of the form

$$H = \sum_{j \in \Lambda} T_j(h), \quad (1)$$

137 where T_j is the translation operator on the lattice Λ , and h is a generic k -local Hamiltonian,
 138 i.e., it includes an arbitrary number of operators acting on lattice sites at most at a (lattice)

139 distance k from a reference lattice point. Such a situation is very common in condensed matter
 140 physics, to say the least. To this aim, we employ the variational principle

$$\frac{\langle \psi | H | \psi \rangle}{\langle \psi | \psi \rangle} \geq E_0 \quad \forall |\psi\rangle, \quad (2)$$

141 and use an energy gradient with respect to the tensor coefficients to search for the minimum
 142 – the precise optimization strategy being discussed later. Such an energy gradient is accessed
 143 by means of tools from *automatic differentiation* (AD), a set of techniques to evaluate the
 144 derivative of a function specified by a computer program that will be summarized below. Since
 145 we directly target systems in the thermodynamic limit, a *corner transfer matrix renormalization*
 146 *group* (CTMRG) procedure constitutes the backbone of the algorithm, and also will come in
 147 handy for AD purposes. This is used to compute the approximate contraction of the infinite
 148 lattice, which is crucial in order to compute accurate expectation values in the first place.
 149 Importantly, the CTMRG routine is *always* performed on a regular square lattice, for which it
 150 can be conveniently defined. Support for other lattices, also non-bipartite ones, is possible by
 151 different lattice mappings, as we will demonstrate.

152 Besides the CTMRG procedure, other well-controlled numerical methods have been devel-
 153 oped to contract the infinite PEPS network. These include boundary matrix product states [22,
 154 59] and tensor coarse-graining techniques [27–30]. These methods can be equally success-
 155 fully combined with the concept of automatic differentiation [37, 47] and provide competitive
 156 results. While other methods can be generalized to non-trivial unit cells [60] as well, in this
 157 work we focus on the CTMRG method due to its straightforward generalization and flexibility
 158 in handling arbitrary unit cells of size (L_x, L_y) . Furthermore, the CTMRG method provides a
 159 robust agnosticism towards possible non-Hermitian transfer operators, which has to be treated
 160 with more care in, e.g., boundary MPS methods.

161 The method we will present in this section gives rise to an upper bound of the ground
 162 state energy in the sense of the variational principle as stated in Eq. (2). But we wish to point
 163 out at this point that for that to be strictly true it would be necessary to choose the CTMRG
 164 refinement parameter χ_E , introduced in detail in Sec. 2.2, to be $\chi_E \rightarrow \infty$. However, in practice
 165 we increase this refinement parameter χ_E until all observables are converged.

166 2.1 iPEPS setup

167 As introduced in the last section, we aim to simulate quantum many-body systems directly in
 168 the thermodynamic limit. To this end, we consider a unit cell of lattice sites that is repeated
 169 periodically over the infinite two-dimensional lattice. Reflecting this, the general configura-
 170 tions of the iPEPS ansatz are defined with an arbitrary unit cell of size (L_x, L_y) on the square
 171 lattice. The lattice setup, denoted by \mathcal{L} , can be specified by a single matrix, which uniquely
 172 determines the different lattice sites as well as their arrangement. Let us consider a concrete
 173 example of an $(L_x, L_y) = (2, 2)$ state with only two and all four individual tensors, denoted by

$$\mathcal{L}_1 = \begin{pmatrix} A & B \\ B & A \end{pmatrix}, \quad \mathcal{L}_2 = \begin{pmatrix} A & C \\ B & D \end{pmatrix}. \quad (3)$$

174 The corresponding iPEPS ansätze are visualized in Fig. 1. Here, the rows/columns of \mathcal{L} cor-
 175 respond to the x/y lattice directions. The unit cell \mathcal{L} is repeated periodically to generate the
 176 full two-dimensional system. As usual, the bulk bond dimension of the iPEPS tensors, denoted
 177 by χ_B , controls the accuracy of the ansatz. An iPEPS state with N different tensors in the unit
 178 cell consists of $Np\chi_B^4$ variational parameters, which we aim to optimize such that the iPEPS
 179 wave function represents an approximation of the ground state of a specific Hamiltonian. The

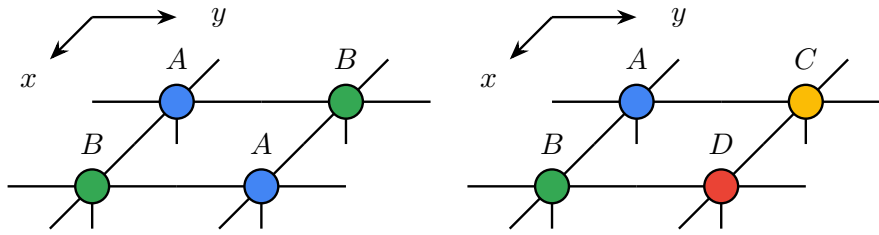


Figure 1: iPEPS ansätze with a unit cell of size $(L_x, L_y) = (2, 2)$ and only two (left) and four (right) different tensors as defined in Eq. (3).

180 parameter p denotes the dimension of the physical Hilbert space, e.g., $p = 2$ for a system of
 181 spin-1/2 particles.

182 The right choice of the unit cell is crucial in order to capture the structure of the targeted
 183 state. A mismatch of the ansatz could not only lead to a bad estimate of the ground state, but
 184 also to no convergence in the CTMRG routine at all. Different lattice configurations have to
 185 be evaluated for specific problems to find the correct pattern.

186 To circumvent the problem of a fixed and a priori chosen unit cell structure, recently an
 187 alternative description to the periodic structure has been proposed [61]. This approach is
 188 applicable if the Hamiltonian has a certain global symmetry, where the additional degree of
 189 freedom can be employed to reduce the description of the state to a subspace, e.g. $SU(2)$ for
 190 spin-1/2 systems. Here the state is described by the smallest possible unit cell, i.e. a single site
 191 for a square lattice, as well as a product of local unitary operators parameterized by a wave
 192 vector $\mathbf{k} = (k_x, k_y)$. A fixed choice of the wave vector then corresponds to the specification
 193 of a unit cell structure in the common iPEPS setup. This approach allows for a variational
 194 optimization of the wave vector along with the translationally invariant iPEPS tensor, removing
 195 the need to choose a fixed unit cell structure altogether.

196 In this work we restrict the description of the method to the common iPEPS setup with
 197 not only trivial unit cells. This enables the adaption of the framework to arbitrary, in general
 198 non-symmetric Hamiltonian models.

199 2.2 CTMRG backbone

200 One major drawback of two-dimensional TNs such as iPEPS is that the contraction of the
 201 full lattice can only be computed approximately. This is due to complexity theoretic obstruc-
 202 tions [19,20] and – practically speaking – the lack of a canonical form, which can only be found
 203 in loop-free tensor networks, for instance in matrix product states [8]. In order to circumvent
 204 the unfeasible exact contraction of the infinite 2d lattice, we employ an approximation scheme,
 205 the directional *corner transfer matrix renormalization group* (CTMRG) routine for iPEPS states
 206 with arbitrary unit cells of size (L_x, L_y) . The CTMRG method approximates the calculation
 207 of the norm $\langle \psi | \psi \rangle$ of the quantum state on the infinite square lattice by a set of effective
 208 environment tensors. This is achieved by an iterative coarse-graining procedure, in which all
 209 (local) iPEPS tensors in the unit cell \mathcal{L} are successively absorbed into the environment ten-
 210 sors towards all lattice directions, until the environment converges to a fixed-point. We will
 211 present a summary of the directional CTMRG methods for an arbitrary unit cell, following
 212 the state-of-the-art procedure [62–64]. The effective environment is displayed in Fig. 2, here
 213 for simplicity for a square lattice with a single-site unit cell $\mathcal{L} = (A)$. It consists of a set of
 214 eight fixed-point tensors, four corner tensors $\{C_1, C_2, C_3, C_4\}$ as well as four transfer tensors
 215 $\{T_1, T_2, T_3, T_4\}$, the latter sometimes also called edge tensors. In case of a larger unit cell, such
 216 a set of eight environment tensors is computed for each individually specified iPEPS tensor in
 217 the unit cell. The unavoidable approximations in the environment calculations are controlled

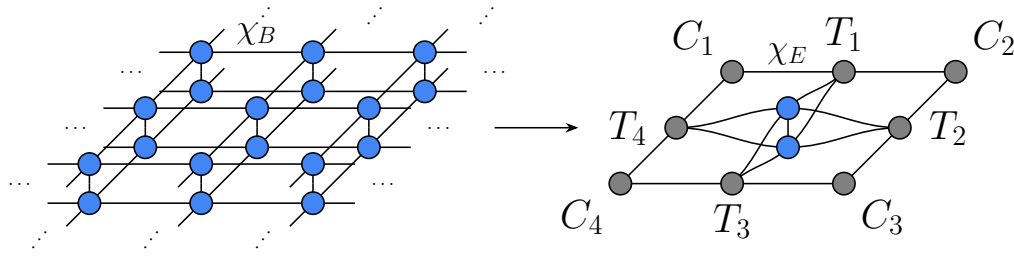


Figure 2: The norm of an iPEPS (here with a single-site unit cell) at a bulk bond dimension χ_B is approximated by a set of eight fixed-point environment tensors. The environment bond dimension χ_E controls the approximations in the CTMRG routine.

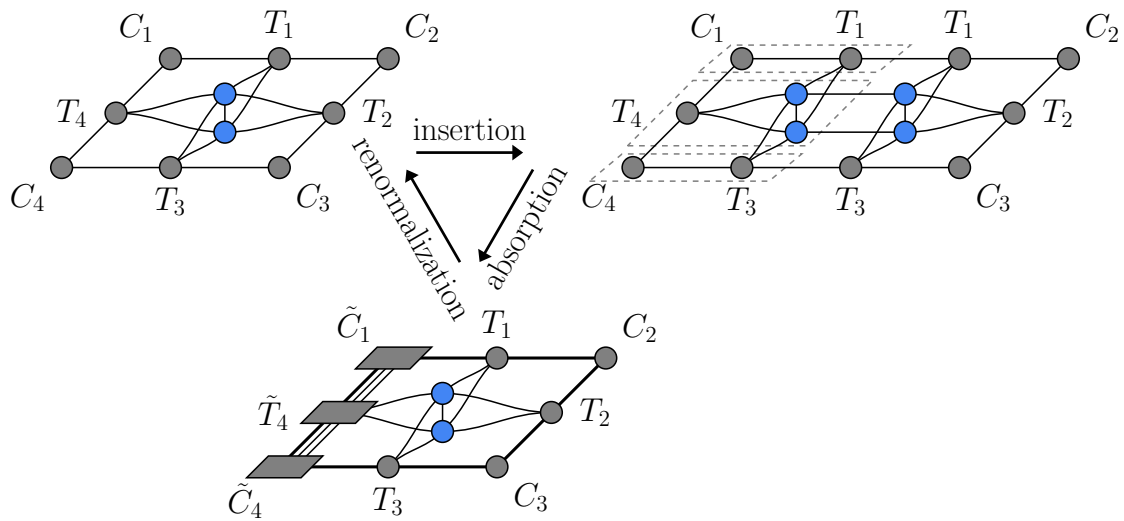


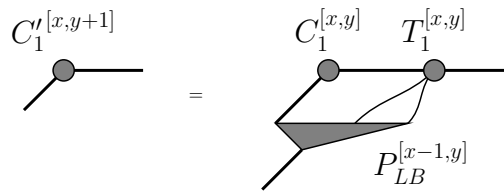
Figure 3: Main steps of a left CTMRG move. One column of tensors is inserted into the network. Upon absorption of these tensors, the environment bond dimension grows rapidly, requiring a renormalisation step.

218 by a second refinement parameter, the environment bond dimension χ_E .

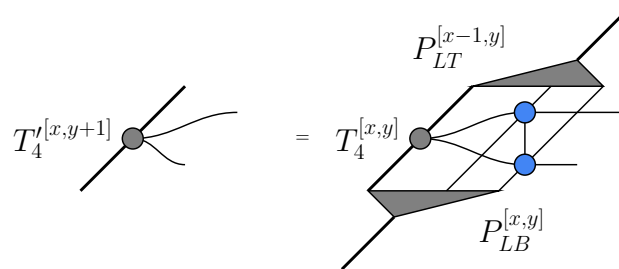
219 In one full CTMRG step, the complete iPEPS unit cell is absorbed into the four lattice di-
 220 rections, such that the eight CTMRG tensors are updated for every iPEPS tensor. This is done
 221 column-by-column or row-by-row, depending on the direction. In each absorption step the
 222 environment bond dimension χ_E grows by a factor of χ_B^2 . To avoid an exponential increase
 223 in memory consumption and computation time, we need a method to truncate the bond di-
 224 mension back to χ_E . In order to do this, we calculate renormalization projectors for each row
 225 or column. Projectors are computed from a suitable patch of the iPEPS state including the
 226 effective environments, to find a best-possible truncation of the bond dimension. Different ap-
 227 proaches for their calculations have been proposed in the literature, which we will discuss in
 228 detail below, especially in the context of AD. In the following description of the CTMRG proce-
 229 dure we focus on a left absorption move, which grows all left environment tensors $\{C_4, T_4, C_1\}$.
 230 The main steps of insertion, absorption and renormalization are shown in Fig. 3. In Sec. 2.2.1,
 231 we will explain the full absorption procedure including renormalization, as it is done in prac-
 232 tise. Although projectors need to be calculated before the absorption, their motivation and the
 233 calculation of different projects is discussed later in Sec. 2.2.2.

234 **2.2.1 Absorption of iPEPS tensors**

235 In order to generate the CTMRG environment tensors, such that they converge to a fixed-
 236 point eventually, the iPEPS tensors are absorbed into them. To this end, we start with the
 237 network of one iPEPS tensor in the unit cell and its accompanying environment tensors. This
 238 is depicted in Fig. 3 in the top left. As shown on the top right of this figure, the network
 239 is extended by inserting one column, consisting of an iPEPS tensor and the top and bottom
 240 transfer tensors. While we depict the case of a single-site unit cell in Fig. 3, we note that
 241 the column of tensors to be inserted is generally dictated by the unit cell structure of the
 242 iPEPS ansatz, i.e., the left neighbor with the corresponding environment tensors for a left
 243 move. This crucial positional information for multi-site unit cells is specified by the coordinate
 244 superscripts in the descriptions below. As indicated by the dashed line in Fig. 3, we absorb
 245 the inserted column into the left environment tensors by contracting all left pointing edges.
 246 This yields new environment tensors whose bond dimensions have grown by a factor χ_B^2 due
 247 to the virtual iPEPS indices, thus we need a way to truncate the dimension back to the CTMRG
 248 refinement parameter χ_E . This is done using the projectors we will discuss and compute in
 249 the next section. For now we introduce them as abstract objects labeled P that implement
 250 the dimensional reduction (i.e., the renormalization step) in an approximate but numerically
 feasible way. The updated tensor C'_1 is then given by the contraction in Fig. 4. As discussed


 Figure 4: Update of the corner tensor C_1 in a left CTMRG step.

251 before, the correct tensors and projectors have to be used in accordance with the periodicity
 252 of the unit cell. The iPEPS tensor is now absorbed into the left transfer matrix T'_4 , where two
 253 projectors are needed to truncate the enlarged environment bond dimension. This is visualized
 254 in Fig. 5. Finally, the lower corner tensor C'_4 is updated, by absorbing a transfer matrix T_3 and


 Figure 5: Update of the transfer matrix T_4 in a left CTMRG step. Here the projectors generally belong to different subspaces, unless the system is one-site translational invariant.

255 using another projector. The three absorption steps in Figs. 4, 5 and 6 are performed for all
 256 rows x at a fixed column y , before moving to the next column $y + 1$. The process of computing
 257 projectors and growing the environment tensors is repeated for each column of the iPEPS unit
 258 cell, until the complete unit cell of $L_x \times L_y$ tensors has been absorbed into the left environment.
 259 This yields updated tensors C'_1 , T'_4 and C'_4 for all $[x, y]$.

261 The absorption of a full unit cell is then performed for the other three directions. In a top
 262 move the tensors C_1 , T_1 and C_2 are grown, in a right move the tensors C_2 , T_2 and C_3 and in

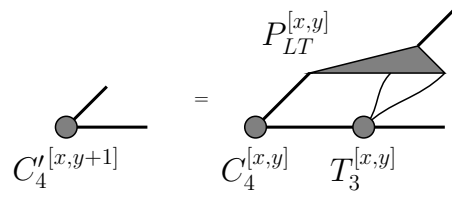


Figure 6: Update of the corner tensor C_4 in a left CTM step.

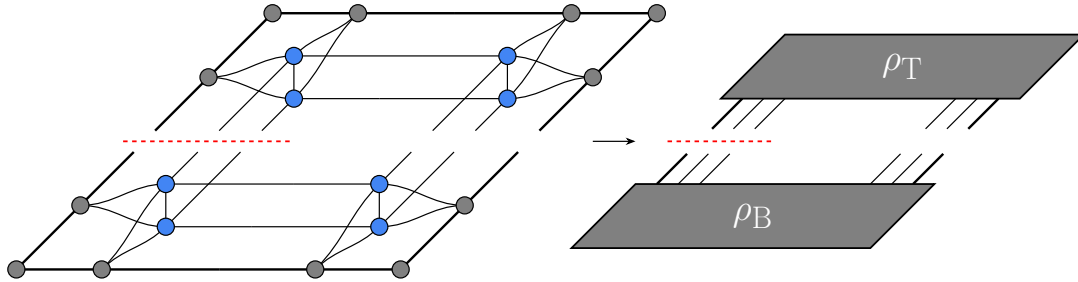


Figure 7: Network of 2×2 iPEPS tensors and the corresponding CTMRG tensors, used as a starting point to compute the truncation projectors. For a left CTMRG step the top and bottom part is contracted into the matrices ρ_T and ρ_B with dimension $(\chi_E \chi_B^2) \times (\chi_E \chi_B^2)$. The red dashed line indicates the bonds that are renormalized back to a bond dimension χ_E .

263 a bottom move the tensors C_3 , T_3 and C_4 . This completes a *single* CTMRG step, which is then
 264 repeated in the directional procedure until convergence is reached. In Sec. 2.2.3 we discuss
 265 appropriate convergence measures.

266 2.2.2 Calculation of projectors

267 In order to avoid an exponential increase of the bond dimension while growing the environ-
 268 ment tensors, projectors are introduced to keep the bond dimension at a maximal value of
 269 χ_E . Here, we will describe a common scheme to compute those projectors [63] and discuss
 270 some properties of their use in combination with AD [42]. The task of finding good projectors
 271 essentially comes down to finding a basis for the virtual space, whose bond dimension we aim
 272 to reduce, that can be used to distinguish between “more and less important” sub-spaces. This
 273 way, we can ideally reduce the dimension while keeping the most important sub-space. In
 274 what follows, we consider the lattice environment of the virtual space that we aim to truncate
 275 using the CTMRG environment tensors. To this end, we use a *singular value decomposition*
 276 (SVD) to identify the basis, in which the bond is optimally truncated such that we keep the
 277 most relevant information of this lattice environment. The lattice environment that we con-
 278 sider is shown in Fig. 7, where the red dotted line identifies the bonds that we aim to optimally
 279 truncate, illustrated for the example of a left absorption step. The arrangement of the tensors
 280 in the network of Fig. 7 follows the unit cell definition \mathcal{L} . For the trivial, single-site unit cell
 281 $\mathcal{L} = (A)$, all four iPEPS tensors are the same. We note that for a larger unit cell, cf. Fig. 1, the
 282 iPEPS tensors and their adjacent environments have to be chosen according to its periodicity.
 283 This setup for the arrangement is favorable, since it incorporates the (approximated) effect of
 284 the infinite environment by including all CTM tensors for the different lattice directions.

285 The projectors are used to renormalize the three left open tensor indices with combined
 286 bond dimension $\chi_E \chi_B^2$ back to the environment bond dimension χ_E in a left absorption step.

287 In order to compute them, we start by defining the matrix

$$\mathcal{M} = \rho_B \cdot \rho_T \quad (4)$$

288 that represents the lattice environment of the virtual bond that we would like to truncate, as
289 visualized in Fig. 8.

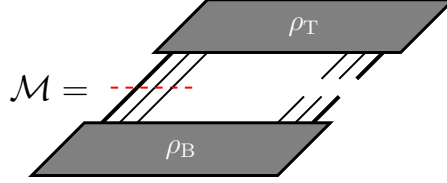


Figure 8: Matrix \mathcal{M} as defined by Eq. (4) in graphical TN notation. The red dashed line indicates the bonds that are renormalized back to a bond dimension χ_E .

290 The procedure outlined here aims to find projectors P_{LT} and P_{LB} , such that the truncated
291 matrix

$$\mathcal{M}_{\text{trunc}} = \rho_B \cdot P_{LT} \cdot P_{LB} \cdot \rho_T, \quad (5)$$

292 is an optimal approximation to \mathcal{M} . To achieve this, we perform a singular value decomposition
293 on \mathcal{M} , i.e.,

$$\mathcal{M} = U_L S_L V_L^\dagger. \quad (6)$$

294 This factorization introduces a basis which allows for a separation of more relevant and less
295 relevant sub-spaces. To this end, we choose the largest χ_E singular values and their corre-
296 sponding singular vectors for the construction of the projectors. Furthermore, we define

$$S_L^+ = \text{inv}(\sqrt{S_L}), \quad (7)$$

297 where a pseudo-inverse with a certain tolerance is used. To increase the numerical stability, a
298 threshold of typically 10^{-6} (corresponding to a threshold of 10^{-12} for the singular values) is
299 used. Smaller singular values are set to zero. The use of a pseudo-inverse in the generation
300 of the projectors is equivalent to the construction of a projector with lower environment bond
301 dimension. Finally, the projectors to renormalize the left absorption step are constructed as

$$\begin{aligned} P_{LT} &= \rho_T \cdot V_L \cdot S_L^+, \\ P_{LB} &= S_L^+ \cdot U_L^\dagger \cdot \rho_B. \end{aligned} \quad (8)$$

302 Here ρ_T and ρ_B again denote the top and bottom part of \mathcal{M} as introduced in Fig. 7. We
303 would like to point out the fact that without a truncation in the SVD above, the product of the
304 projectors we create in this way assembles the identity

$$\begin{aligned} P_{LT} \cdot P_{LB} &= \rho_T \cdot V_L \cdot S_L^{-1} \cdot U_L^\dagger \cdot \rho_B \\ &= \rho_T \cdot (\rho_B \cdot \rho_T)^{-1} \cdot \rho_B = \mathbb{1}. \end{aligned} \quad (9)$$

305 We stress again, that the choice of truncation in the calculations of the projectors is optimal in
306 order to approximate the lattice environment \mathcal{M} . A graphical representation of these projec-
307 tors is given in Fig. 9.

308 During a left-move, described in the previous section, we absorb the iPEPS tensors in the
309 unit cell column-by-column into the left environments. A renormalization step is required for

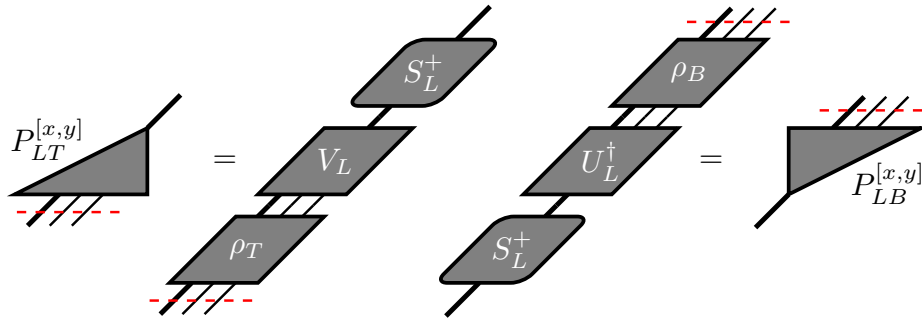


Figure 9: Calculation of top and bottom projectors for a left CTMRG absorption step. The red dashed line indicates the bonds that are renormalized back to a bond dimension χ_E .

310 each of those moves, resulting in projectors that are specific to every bond. We therefore label
 311 them by the positions in the unit cell, i.e., $P_{LT}^{[x,y]}$ and $P_{LB}^{[x,y]}$.

312 The process to generate the projectors described above uses the full lattice environment
 313 \mathcal{M} , and thus we call them *full projectors*. It should be noted that Fishman et al. have proposed
 314 a scheme to calculate equivalent projectors in a fashion that is numerically more stable, at the
 315 cost of being computationally more expensive [64]. Their method is particularly useful in the
 316 case of a singular value spectrum of \mathcal{M} that decays very fast.

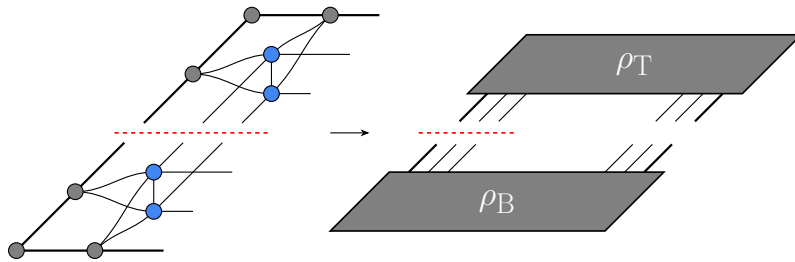


Figure 10: Network of 2×1 iPEPS tensor and the corresponding CTMRG tensors, which is used as a reduced network to calculate the half projectors for a left CTMRG step. The red dashed line indicates the bonds that are renormalized back to a bond dimension χ_E .

317 Finally, different lattice environments of the virtual bond in question can be used to gener-
 318 ate projectors. A very practical version are the so called *half projectors*. For those we choose a
 319 lattice environment as illustrated in Fig. 10. These projectors are computationally less costly,
 320 as they require a smaller network to be contracted. They only take into account correlation
 321 within one half of the network, however this proves to be sufficient in many different applica-
 322 tions. Lately, there have been proposals for even cheaper alternatives of lattice environments
 323 and projector calculations [65], which yet have to be tested in the context of automatic differ-
 324 entiation and variational iPEPS optimization.

325 2.2.3 Convergence and CTMRG fixed-points

326 The CTMRG routine as described above is a power-method that eventually converges to a
 327 fixed-point. At this fixed-point, the set of environment tensors describes the contraction of
 328 the infinite lattice with an approximation controlled by the environment bond dimension χ_E .
 329 Convergence of the CTMRG tensors to the fixed-point can be monitored in different ways.
 330 In regular applications (those that do not involve automatic differentiation and gradients) the

331 singular value spectrum of the corner tensors is typically a good quantity. Once the norm differ-
 332 ence of the spectrum between two successive CTM steps converges below a certain threshold,
 333 the environment tensors are assumed to be converged.

334 One peculiarity that is however not incorporated in this convergence check is sign or phase
 335 fluctuation for real or complex tensor entries, respectively. This means that, while projectors
 336 and hence the CTMRG tensors converge in absolute value, their entries can have different
 337 signs/phases in consecutive CTM steps. For reasons that become clear in Sec. 2.5 it is however
 338 required to reach *element-wise convergence* in the environment tensors for them to represent
 339 an actual fixed-point [42]. Those fluctuations originate from the gauge freedom in the SVD
 340 performed in Eq. (6). This is reflected in the freedom of introducing a unitary (block-)diagonal
 341 matrix Γ in an SVD,

$$\mathcal{M} = USV^\dagger = (U\Gamma)S(\Gamma^\dagger V^\dagger), \quad (10)$$

342 which leaves the expression invariant. The gauge freedom from the SVD directly affects the cal-
 343 culation of the projectors, such that we aim to fix the phases while computing these projectors.
 344 By eliminating this gauge freedom, at the true fixed-point, both projectors and environment
 345 tensors should be converged element-wise.

346 To fix the gauge, we introduce a diagonal unitary matrix Γ that redefines the phase of
 347 the largest entry (in absolute value) of every left singular vector to place it on the positive
 348 real axis [42]. To avoid instabilities of this gauge-fixing procedure due to numerical quasi-
 349 degeneracies, we always pick the first of such largest elements in basis order. Other choices,
 350 like addressing the first element with magnitude above a fixed threshold, are also possible.
 351 We further note that an alternative scheme to archive a fixed point in the CTMRG has recently
 352 been proposed [66].

353 2.3 Energy expectation values

354 Computing the energy expectation value required for the energy minimization is straightfor-
 355 ward using the CTMRG environment tensors. Assuming a Hamiltonian with only nearest-
 356 neighbour interaction terms, individual bond energies can be computed as shown in Fig. 11.
 357 The full energy expectation value, $\langle \psi | H | \psi \rangle / \langle \psi | \psi \rangle$, is obtained by collecting all different en-
 358 ergy contributions, i.e., all different terms in the Hamiltonian. Longer-range interaction can
 359 be treated as well, by simply enlarging the diagrams of Fig. 11 and performing more expensive
 360 contractions, which however occur only once per optimization step. In order to formulate a
 361 variational optimization of the tensor coefficients parametrizing the wave function, a gradient
 362 for the energy expectation value – including the foregone fixed-point CTMRG routine – is re-
 363 quired. This is achieved by the concept of automatic differentiation, as we will describe next.

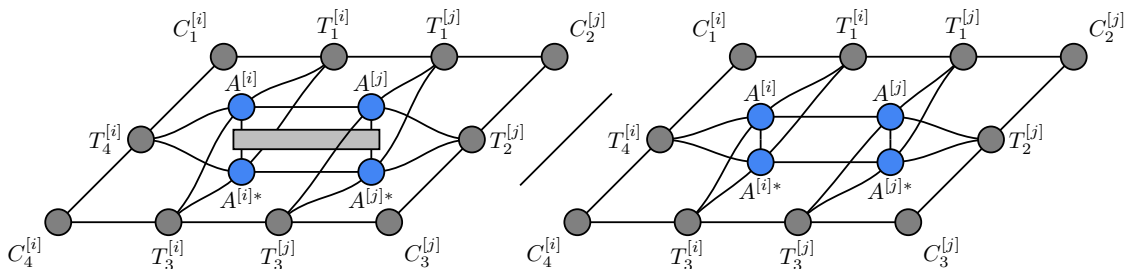


Figure 11: Expectation values of a (horizontal) nearest-neighbour Hamiltonian term $\langle \psi | h_{i,j} | \psi \rangle / \langle \psi | \psi \rangle$ in tensor network notation, using the fixed-point CTMRG environments.

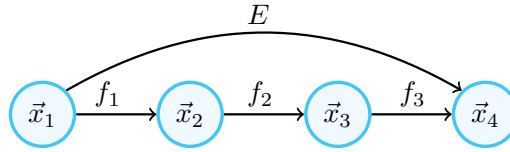
365 **2.4 Automatic differentiation**

Figure 12: Example of a computational graph for the function decomposition in Eq. (11).

366 *Automatic differentiation* (AD), sometimes also referred to as *algorithmic differentiation* or
 367 *automated differentiation*, is a method for taking the derivative of a complicated function which
 368 is evaluated by some computer algorithm. It has been an important tool for optimization tasks
 369 in machine learning for many years. An introduction can be found in e.g. Ref. [67]. After
 370 its initial introduction in a foundational work [37], AD has found increasing applications in
 371 numerical TN algorithms in recent years [38, 39, 41, 42, 44, 45]. For the sake of simplicity,
 372 let us consider a function $E : \mathbb{R}^n \rightarrow \mathbb{R}^m$ for which we would like to evaluate the deriva-
 373 tive. Noticeably, extensions to complex numbers are possible, and we provide some additional
 374 comments in Appendix B. We have the particular use-case of the energy expectation value
 375 $E(|\psi\rangle) = \langle \psi | H | \psi \rangle / \langle \psi | \psi \rangle$ of an iPEPS in mind, in which case the co-domain of the function
 376 E is \mathbb{R} . As we explain below, this has some important consequences for the use of AD.

377 Automatic differentiation makes use of the fact that many functions and algorithms are
 378 fundamentally built by concatenating elementary operations and functions like addition, mul-
 379 tiplication, projection, exponentiation and taking powers, whose derivatives are known. The
 380 central insight is now that we can build up the gradient of a more complicated function from
 381 the derivatives of its elementary constituents by the *chain rule of differentiation*. In principle
 382 this even allows for a computation of the gradient to machine precision. It should be noted
 383 however, that it is neither necessary nor useful to deconstruct every function into its most
 384 elementary parts. Rather it is advantageous to deconstruct the function at hand only into a
 385 minimal amount of constituent-functions for which a derivative can be determined. These
 386 functions are often referred to as the *primitives* of the function of interest E . Primitives might
 387 themselves be a composition of many constituents but the derivative of the primitives them-
 388 selves is known as a whole. An illustrative example for a primitive is a function that takes
 389 two matrices as an input and outputs the multiplication of them. On an elementary level this
 390 function is composed out of many multiplications and additions, but one can write down the
 391 derivative w.r.t. its inputs immediately. The choice of primitives describes the level of coarse-
 392 ness on which the AD process needs to know the details of the function E to compute the
 393 desired gradient. Defining large primitives of a function can reduce memory consumption, as
 394 well as increase performance and numerical stability of the AD process, e.g., by avoiding spuri-
 395 ous divergences. Once the high-level function E has been decomposed into its minimal number
 396 of primitives, we can represent this decomposition with a so called *computational graph*. The
 397 computational graph is a directed, a-cyclic graph whose vertices represent the data generated
 398 as intermediate results by the primitives and the edges represent the primitives themselves,
 399 that transform the data from input to output.

400 As an example let us suppose we are able to decompose the function E into three primitives
 401 f_1, f_2 and f_3 , such that $E = f_3 \circ f_2 \circ f_1$. The primitives are maps between intermediate spaces

$$E : \mathbb{R}^{n_1} \xrightarrow{f_1} \mathbb{R}^{n_2} \xrightarrow{f_2} \mathbb{R}^{n_3} \xrightarrow{f_3} \mathbb{R}^{n_4} \quad (11)$$

402 and we refer to the variables in these spaces as $\vec{x}_i \in \mathbb{R}^{n_i}$. The computation graph illustrating
 403 this situation is shown in Fig. 12. AD can be performed in two distinct schemes, often called

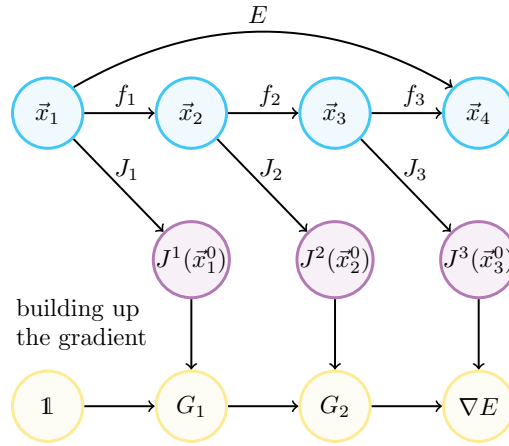


Figure 13: Illustration of forward-mode AD as described in Eq. (14) for the function decomposition in Eq. (11).

404 *forward-* and *backward-mode* AD. In the following we will demonstrate the two AD modes with
 405 the example of our previously introduced function E and its primitives. This will also serve to
 406 illustrate the computational cost of these AD schemes for the iPEPS use-case. Since f_1, f_2 and
 407 f_3 are said to be primitives, their Jacobians

$$J^i : \mathbb{R}^{n_i} \rightarrow \mathbb{R}^{n_{i+1}} \times \mathbb{R}^{n_i},$$

$$J^i(\vec{x}_i^0) = \left(\frac{\partial f_i}{\partial \vec{x}_i} \right) \Big|_{\vec{x}_i = \vec{x}_i^0} \quad (12)$$

408 are known. An AD evaluation of the gradient of E at a specific point \vec{x}_1^0 is then given by the
 409 chain rule, the concatenation of the Jacobians of the primitives

$$\nabla E(\vec{x}_1^0) = J^3(\vec{x}_3^0) \cdot J^2(\vec{x}_2^0) \cdot J^1(\vec{x}_1^0), \quad (13)$$

410 with $f_i(\vec{x}_i^0) = \vec{x}_{i+1}^0$. The difference between the *forward-* and *backward-mode AD* essentially
 411 comes down to the question from which side we perform the multiplication of the Jacobians
 412 above.

413 In the *forward-mode AD* scheme, the gradient is built up simultaneously with the evaluation
 414 of the primitives f_1, f_2 and f_3 , according to the prescription

$$f_i(\vec{x}_i^0) = \vec{x}_{i+1}^0,$$

$$G_i = J^i(\vec{x}_i^0) \cdot G_{i-1} \quad (14)$$

415 for the i -th step, with the starting condition $G_0 := \mathbb{1}_{n_1 \times n_1}$ and with the final result that is given
 416 by $G_3 = \nabla E(\vec{x}_1^0) \in \mathbb{R}^{n_4 \times n_1}$. We see that in this case we build up Eq. (13) from right to left
 417 or “along the computational graph” as illustrated in Fig. 13. At first sight, such a procedure
 418 offers the potential advantage of not requiring to store intermediate results of the primitives
 419 in memory. However, if the dimension of the input (domain of E) is much larger than the
 420 dimension of the output (co-domain of E) – as it is the case in our use-case of iPEPS – this
 421 procedure becomes computationally very heavy. Indeed, saving and multiplying the large
 422 Jacobians in Eqs. (14) is often impractical. Thus, it is common to split up the starting condition
 423 $G_0 := \mathbb{1}_{n_1 \times n_1}$ into the n_1 canonical basis vectors $\{\vec{e}_i\}_{i=1, \dots, n_1}$. The procedure to generate the
 424 gradient from Eq. (14) is then repeated n_1 times, each iteration generating a single component
 425 i . In this case, each step of the process of generating a component of the gradient is done by
 426 calculating a *Jacobian-vector product* (JVP), so that only the resulting vector has to be stored.

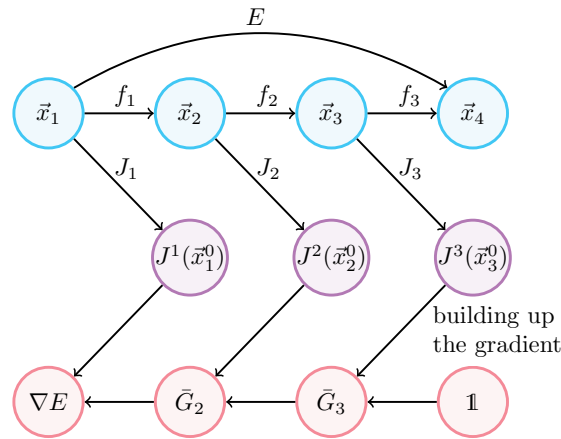


Figure 14: Illustration of backward-mode AD as described in Eq. (15) for the function decomposition in Eq. (11).

427 In order to create the full gradient in this way we need to repeat the procedure n_1 times, and
 428 the cost of calculating the full gradient scales as $\mathcal{O}(n_1) \times \mathcal{O}(E)$, where $\mathcal{O}(E)$ is the cost of
 429 evaluating E .

430 The *backward-mode* AD scheme works instead by first evaluating the function E and storing
 431 all intermediate results of the primitives along the way, and by then applying the iterative
 432 prescription

$$\bar{G}_i = \bar{G}_{i+1} \cdot J^i(\bar{x}_i^0) \quad (15)$$

433 with the starting condition $\bar{G}_4 = \mathbb{1}_{n_4 \times n_4}$ and the final result $\bar{G}_1 = \nabla E(\bar{x}_1^0) \in \mathbb{R}^{n_4 \times n_1}$. In the
 434 AD literature the objects \bar{G}_i are called adjoint variables and the functions that map the ad-
 435 joint variable on to each other, defined by Eq. (15), are called adjoint functions. We refer
 436 to Appendix A for more details on the adjoint functions and adjoint variables. In some parts
 437 of the literature the adjoint functions are also called pullbacks, which can be understood by
 438 looking at AD in language of differential geometry, cf. Appendix D. We see that in this case we
 439 build up Eq. (13) from left to right or as graphically illustrated in Fig. 14. This scheme has
 440 the advantage of being computationally much cheaper if the output (co-domain) dimension is
 441 smaller than the input (domain) dimension – precisely the situation of our iPEPS setup, with
 442 $n_1 = Np\chi_B^4$ and $n_4 = 1$. We indeed only need to compute *vector-Jacobian products* (VJP) when
 443 evaluating the gradient, and, moreover, the full gradient is computed at once, instead of just
 444 a single element at a time as in the forward-mode AD scheme. This is why the cost of calcu-
 445 lating the gradient of the energy expectation value with *backwards-mode* AD is $\mathcal{O}(1) \times \mathcal{O}(E)$,
 446 which is superior to the cost of *forward-mode* AD. However, since we need to save all inter-
 447 mediate results of the primitives along the way in order to compute the gradient, the memory
 448 requirement for this scheme is in principle unbounded. Fortunately, the fixed-point condition
 449 for the iPEPS environments can be used to guarantee that the memory remains bounded in
 450 our calculations, as we illustrate in the following section.

451 2.5 Calculation of the gradient at the CTMRG fixed-point

452 Computationally, the CTMRG routine represents the bottleneck of the full iPEPS energy func-
 453 tion. It involves many expensive contractions and SVDs. Moreover, it requires an a priori
 454 unknown number of CTMRG iterations to reach convergence of the environment tensors. This
 455 would be especially disadvantageous for the gradient evaluation using plain-vanilla backward-
 456 mode AD, since this would require unrolling all the performed CTMRG iterations and paying
 457 a memory consumption linear in their number. However, this can be avoided by leveraging

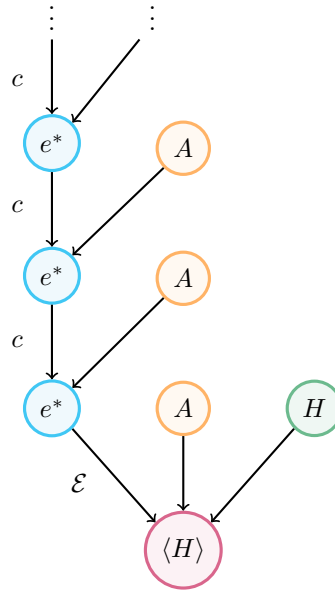


Figure 15: Computational graph of the CTMRG procedure for calculating the energy density at fixed point.

458 that fact that the CTMRG iteration eventually converges to a fixed point, and this is precisely
 459 the condition under which the energy evaluation is then performed. As soon this fixed point
 460 is reached, all CTMRG iterations are identical, i.e., reproducing the converged environment
 461 tensors. We can, in this situation, get away with only saving intermediate results from such a
 462 converged CTMRG iteration. This reduces the memory requirements by a factor of the number
 463 of CTMRG iterations that we perform [37]. We stress here that, for this approach to work,
 464 we must make sure that the CTMRG procedure reaches an actual fixed point, meaning that
 465 all CTMRG environment tensors are converged element wise as discussed in Sec. 2.2.3. The
 466 fixed-point equation can be written as

$$e^*(A) = c(A, e^*(A)), \quad (16)$$

467 where the function c is one full CTMRG iteration, A are the iPEPS tensors which are constant
 468 during the CTMRG procedure and $e^*(A)$ represents the CTMRG environment tensors at the
 469 fixed-point. \mathcal{E} is the function that maps the iPEPS tensors with the fixed point environment
 470 tensors and the Hamiltonian operators to the energy expectation value. The computational
 471 graph for the ground state energy is illustrated in Fig. 15. From it we can construct the form
 472 of the gradient of the energy expectation value with respect to the parameters of the iPEPS
 473 tensors A ,

$$\frac{\partial \langle H \rangle}{\partial A} = \frac{\partial \mathcal{E}}{\partial A} + \frac{\partial \mathcal{E}}{\partial e^*} \sum_{n=0}^{\infty} \left(\frac{\partial c}{\partial e^*} \right)^n \frac{\partial c}{\partial A}. \quad (17)$$

474 In practice this infinite sum is evaluated to finite order until the resulting gradient is converged
 475 to finite accuracy. An alternative viewpoint on the gradient at the fixed-point of the CTMRG
 476 procedure is presented in the Appendix C. It has recently been noted in Ref. [66] that the sta-
 477 bility and accuracy of the SVD derivative can be improved by including a previously neglected
 478 gradient contribution from the truncated part of the singular value spectrum.

479 2.6 Optimization

480 As discussed in the introduction of Sec. 2 we seek to find the iPEPS approximation $|\psi\rangle_{\text{TN}}$ of the
 481 ground state vector $|\psi_0\rangle$. Employing the methods discussed in the last sections we can describe
 482 this energy calculation as function $E(|\psi\rangle_{\text{TN}})$, consisting of the CTMRG power-method and the
 483 expectation value approximation using the resulting CTMRG environment tensors. Since we
 484 can calculate the gradient $\nabla E(|\psi\rangle_{\text{TN}})$ of this real scalar function it is straightforward to use
 485 well-known optimization methods to find the energy minimum. We would like to stress that
 486 the state vector $|\psi\rangle_{\text{TN}}$, and thus the energy function, only depends on the tensors defining
 487 the iPEPS ansatz and not the environment tensors since they are implicitly calculated from
 488 the ansatz. In this discussion we focus on two types of methods based on the gradient: The
 489 (*nonlinear*) *conjugate gradient* (CG) [68–72] and the quasi-Newton methods [73–78].

490 A naive approach to find the minimum of a function $E(|\psi_i\rangle)$, of which the gradient $\nabla E(|\psi_i\rangle)$
 491 is known, is to shift the input parameters $|\psi_i\rangle$ sufficiently along the negative gradient so that
 492 we find a new position $|\psi_{i+1}\rangle$ where the function value is reduced. At the end of this section
 493 we discuss what a sufficient step size means in this context. Iterating this procedure to a point
 494 where the gradient of the function vanishes (within a pre-defined tolerance) yields a solution
 495 to the optimisation problem. Thus either a saddle point or a (local) minimum is reached then.
 496 This method is called steepest gradient descent. Although it resembles one of the simplest
 497 methods to find a descent direction, it is known to have a very slow convergence for difficult
 498 problems, e.g., for functions with narrow valleys [79]. Therefore, we use in practice more
 499 sophisticated methods to determine the descent direction.

500 The family of nonlinear conjugate gradient as generalization of the linear conjugate gra-
 501 dient method modifies this approach. Instead of using the negative gradient as a direction in
 502 each iteration step it uses a descent direction which is conjugated to the previous ones. For
 503 the linear conjugate gradient method there is a known factor β_i to calculate the new descent
 504 direction $d_i = g_i + \beta_i d_{i-1}$ from the gradient g_i of the current step and the descent direction
 505 d_{i-1} of last step. In the generalization for nonlinear functions this parameter is not uniquely
 506 determined anymore, however there are different approaches to estimate this parameter in the
 507 literature [69–71]. In our implementation we chose the nonlinear conjugate gradient method
 508 in the formulation as has been suggested by Hager and Zhang [72],

$$\begin{aligned}
 \tilde{\beta}_i^{\text{HZ}} &= \frac{1}{d_{i-1}^\top y_i} \left(y_i - 2d_{i-1} \frac{\|y_i\|^2}{d_{i-1}^\top y_i} \right)^\top g_i, \\
 \eta_i &= \frac{-1}{\|d_{i-1}\| \min(\eta, \|g_{i-1}\|)}, \\
 \beta_i^{\text{HZ}} &= \max(\tilde{\beta}_i^{\text{HZ}}, \eta_i),
 \end{aligned}
 \tag{18}$$

509 with $\|\cdot\|$ the Euclidian norm, $y_i = g_i - g_{i-1}$ and $\eta > 0$ a numerical control parameter which
 510 has been set to $\eta = 0.01$ in the work by Hager and Zhang. In our tests and benchmarks this
 511 choice for β_i has been proven to be numerically stable.

512 The other family of optimization methods we use in our implementation are the quasi-
 513 Newton methods, concretely the *Broyden–Fletcher–Goldfarb–Shanno* (BFGS) algorithm [75–
 514 78] and its *low-memory* (L-BFGS) variant [74, 80]. These methods are based on the Newton
 515 method where the descent direction is calculated using not only the gradient, but also the
 516 second derivative (the Hessian matrix). Unfortunately, it is computationally expensive to cal-
 517 culate the Hessian for large sets of input parameter, which makes this method only feasible
 518 for small parameter sets (i.e., iPEPS ansätze with a small number of variational parameters).
 519 Quasi-Newton methods solve this problem by not calculating the full Hessian, but an approx-
 520 imation of it. To this end, the gradient information from successive iteration steps is used to

521 update the approximation in each step. The BFGS algorithm stores the full approximated Hessian matrix, including the information from all previous steps. In contrast, the L-BFGS method
 522 calculates the effective descent direction in an iterative manner from the last N optimization
 523 steps. This way not the full (approximated) Hessian has to be stored in memory but only the
 524 gradients of the last N steps. This reduces the memory consumption by an order of magnitude.
 525 The disadvantage is that not the full information of all previous steps is considered, but only
 526 a fraction of it. Nevertheless, due to the memory requirements to store the full approximated
 527 Hessian in the standard BFGS method for larger iPEPS bond dimensions we use L-BFGS as the
 528 default quasi-Newton method.
 529

530 As noted before, we would like to shift the variational parameters x_i along the descent
 531 direction d_i determined by the different algorithms discussed above. With this shift we aim to
 532 find a new ansatz $x_{i+1} = x_i + \alpha_i d_i$ with α_i the step size along the descent direction. Ideally,
 533 we would like to find the optimal step size $\alpha_i = \min_{\alpha} E(x_i + \alpha d_i)$ minimizing the function
 534 value along the descent direction. However, determining this optimal value is computationally
 535 expensive and thus in practice, we stick to a sufficient step size fulfilling some conditions. The
 536 procedure to find this step size is called *line search* [81–84]. In our implementation we use
 537 the Wolfe conditions [82–84], since they guarantee properties which are feasible particularly
 538 for the (L-)BFGS method and its iterative update of the effect of the approximate Hessian.

539 2.7 Handling of physical symmetries

540 One important property of tensor networks is their ability to incorporate physical symmetries,
 541 such as global internal symmetries or spatial symmetries, into their structure exactly. This can
 542 be achieved at the level of each individual tensor, ensuring that the entire many-body wave
 543 function remains symmetry-invariant. On one hand, this approach allows for the targeting of
 544 specific sectors of the Hamiltonian and facilitates a symmetry-resolved analysis of the model
 545 under consideration. On the other hand, it restricts the number of remaining variational pa-
 546 rameters and can lead to a substantial computational speed-up, which, in turn, enables access
 547 to larger bond dimensions.

548 Global symmetries can be implemented by making the tensors quantum number-preserving,
 549 with quantum numbers corresponding to the underlying symmetry group. This results in a
 550 sparse tensor block structure, where linear algebra operations are performed on a generally
 551 larger set of much smaller individual tensors, leading to more efficient manipulations. Com-
 552 mon symmetries exploited in tensor network simulations include Abelian symmetries such as
 553 \mathbb{Z}_N or $U(1)$ [85, 86], non-Abelian symmetries such as $SU(2)$ [87, 88], and also fermionic sym-
 554 metries [89, 90]. Moreover, lattice symmetries can be directly implemented as well, e.g. by
 555 imposing reflection or rotation symmetry for the tensor entries.

556 By making the full set of algorithmic tensor operations, such as tensor initialization, con-
 557 traction, factorization, index permutation, etc., aware of the block structure, symmetric tensors
 558 can be treated analogously to non-symmetric ones on a conceptual level. This includes their
 559 use in variational optimization based on automatic differentiation. There exist several open
 560 source libraries that can handle internal (non)-Abelian and lattice symmetries in TNs [91–94],
 561 some already within the scope of variational PEPS optimization [50].

562 2.8 Pitfalls and practical hints

563 2.8.1 Iterative SVD algorithm

564 We also advertise the use of iterative algorithms for the calculation of the SVD in the CTMRG
 565 procedure. This can be quite advantageous computationally, since only χ_E singular values are
 566 needed for a matrix of size $(\chi_E \chi_B^2) \times (\chi_E \chi_B^2)$ during the CTMRG. To this end we use the use

567 the *Golub-Kahan-Lanczos* (GKL) bidiagonalization algorithm with additional orthogonalization
 568 for the Krylov vectors. This algorithm is available, e.g., in packages like `KRYLOVKIT.JL` [95] or
 569 `ITERATIVESOLVERS.JL` [96] in the `JULIA` programming language. We highlight the utility of this
 570 type of algorithm for the calculation of the SVD with the comparison of the computational
 time of the different algorithms in the iPEPS use case in Fig. 16.

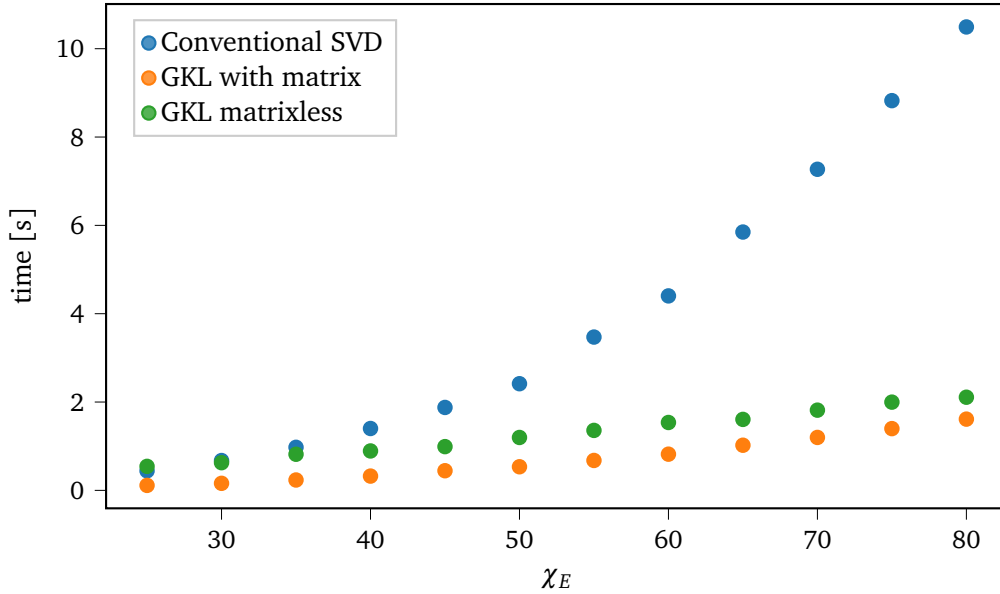


Figure 16: Comparison of the computational time for the calculation of the first χ_E singular values/vectors of a matrix of dimension $(\chi_E \chi_B^2) \times (\chi_E \chi_B^2)$ obtained in a CTMRG procedure with bond dimension $\chi_B = 6$. The conventional SVD (blue), which is truncated only after calculating the full SVD spectrum is substantially slower than the iterative GKL methods. The GKL algorithm in the CTMRG use case was showed comparable performance when constructing the $\chi_E \chi_B^2$ matrix explicitly (orange) or by just implementing its action of a vector (green). While the GKL algorithm for the case at moderate d and χ_E constructing the matrix usually is faster, at larger χ_B and χ_E it can become advantageous to only implement the action of the matrix.

571

572 2.8.2 Stability of the CTMRG routine

573 One of the basic prerequisite for a stable variational iPEPS optimization is a robust CTMRG
 574 routine fulfilling the convergence requirements discussed in Sec. 2.2.3. Obviously, there is
 575 the environment bond dimension χ_E to control the accuracy of the approximation of the envi-
 576 ronment. If the environment bond dimension is chosen too low, the approximation is invalid
 577 and the CTMRG routine can yield an inaccurate result for the expectation value. This could
 578 further lead to an unstable variational update. To check heuristically whether the refinement
 579 parameter χ_E is chosen sufficiently high, one can check the singular value spectrum obtained
 580 during the projector calculation as described in Sec. 2.2.2. As a reliable criteria for the amount
 581 of information loss, we compute the truncation error ε_T given by the norm of the discarded
 582 singular values of the normalized spectrum [97]. If the truncation error is larger than some
 583 threshold (e.g., $\varepsilon_T > 10^{-5}$), one can assume that the environment bond dimension is chosen
 584 too low and has to be increased. Employing this procedure, the bond dimension can automat-
 585 ically be increased during the variational optimization if necessary. A sufficiently large χ_E
 586 is crucial as the AD optimization can otherwise exploit the inaccuracies of the CTMRG procedure,
 587 leading to false ground states with artificially low energy.

588 2.8.3 Prevention of local minima

589 An ideal iPEPS optimization finds the global energy minimum of the input Hamiltonian within
 590 the iPEPS ansatz class of fixed unit cell and bond dimension. In practice, however, it is possible
 591 – and likely – that the algorithm gets stuck in local minima. In order to avoid local minima
 592 and reach the global optimum, there are a number of possible tricks. The naive way is to start
 593 several simulations with different random initial states. This is typically a practicable solution,
 594 although it is not well controllable and requires large computational resources.

595 An optimization of a system with a tendency for local minima might still be successful, if a
 596 suitable initial state is provided. One possibility are initial states obtained by imaginary-time
 597 evolution methods (simple update, full update [22,23,98]). While this is typically a convenient
 598 solution, it is sometimes necessary to perturb the input tensors with a small amount of noise
 599 (e.g., 10^{-2} in relative amplitude) to actually avoid local minima. As an alternative, one can
 600 input a converged state obtained from energy minimization of a different TN ansatz, provided
 601 there is a suitable mapping between the different structures. Examples for this technique are
 602 provided for benchmarks on different lattices in Sec. 4.

603 Finally, the method of perturbing a suitable initial state with small amount of random
 604 noise of course could also be applied to the result of one optimization run. As suggested in
 605 the literature [99], this could help to escape possible local minima. Therefore, one could retry
 606 this method a few times and keep the best result of all runs.

607 2.8.4 Recycling of environments

608 The calculation of the environment tensors with the CTMRG routine is expensive and time
 609 consuming. During an optimization process one can reuse the environment tensors of the
 610 previous optimization step as input for the next. This is advisable in the advanced stages of
 611 the optimization, in which the gradient is already small. In this scenario the iPEPS tensors
 612 usually only change minutely, such that starting the CTMRG routine from the environments
 613 of the last PEPS tensor can reduce the number of CTMRG steps required for convergence
 614 substantially.

615 2.8.5 Analysing iPEPS data at finite bond dimensions

616 Data generated with the variational iPEPS setup inevitably carries finite iPEPS bond dimension
 617 χ_B (or even finite environment bond dimension χ_E) effects. Several schemes are available to
 618 utilize the correlation length of the optimal tensors at a certain value of χ_B to extrapolate
 619 the values of observables [100–102]. Additionally, a extrapolation scheme using data of an
 620 optimized iPEPS state at finite χ_B and finite but suboptimal χ_E has been proposed and shown
 621 useful [103].

622 2.8.6 Degenerate singular values

623 Although very rare, a degenerate singular value spectrum in the calculation of the projec-
 624 tors can be an obstacle. The gradient of the SVD becomes ill-defined in this case, due to terms
 625 $F_{i,j} = 1/(s_j^2 - s_i^2)$ in the derivative [45], where s_i are the singular values. Naturally, it would be
 626 desirable to remove the degeneracy by constraining the system to the correct physical symme-
 627 try, thereby grouping the degenerate singular values to common multiplets of the underlying
 628 symmetry group. If this is not possible or the degeneracies appear independently of a symme-
 629 try (“accidental” degeneracy), workarounds have to be used. One possibility is to add a small
 630 amount of noise in the form of a diagonal matrix XX^{-1} on the CTMRG environment links, with
 631 the elements of X drawn from a tiny interval $[1 - \varepsilon, 1 + \varepsilon]$. This can space out the singular
 632 value spectrum and stabilize the SVD derivative [104]. Recently an alternative procedure to

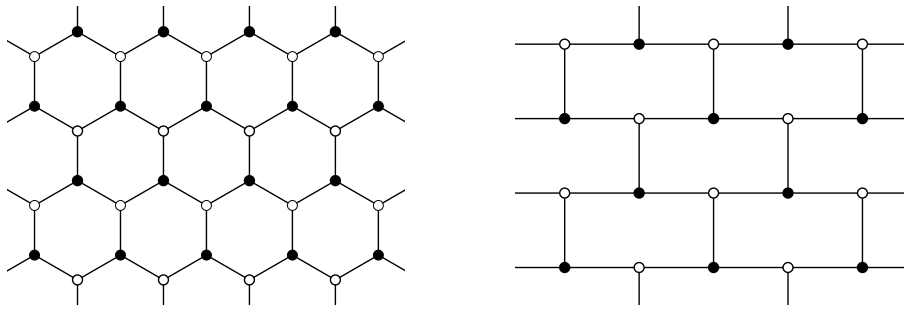


Figure 17: Honeycomb and topologically equivalent brick-wall lattice.

633 eliminate divergences in the derivative of the SVD with degenerate spectrum has been proposed in Ref. [66]. Here, for the case of a rotationally invariant CTMRG, the divergent term
 634 is canceled out by a particular gauge fixing of the environment tensors.
 635

636 3 Extension to other lattices

637 The directional CTMRG routine on the square lattice is very convenient for its orthogonal
 638 lattice vectors and definition of the effective environments. It is therefore natural to exploit
 639 the implemented routines for different kind of lattices that can be mapped back to the square
 640 lattice. This can typically be achieved by a suitable coarse-graining, in which a collection of
 641 lattice sites on the original lattice is mapped into an effective site on the square lattice. Energy
 642 expectation values can then be directly evaluated in the coarse-grained picture as well. This is
 643 even advantageous for the AD optimization procedure, since the energy can often be computed
 644 with a smaller number of individual terms. In this section we will present the mapping for four
 645 types of lattices frequently found in condensed matter systems – the honeycomb, Kagome,
 646 square-Kagome and triangular lattice. Naturally, the framework can be extended by other
 647 suitable two-dimensional lattices, such as dice, square-octagon, maple-leaf and others. As
 648 an alternative to the coarse-graining approach, CTMRG methods that directly operate on the
 649 original lattice structures can also be defined [46, 105, 106].

650 3.1 Honeycomb lattice

651 The honeycomb, hexagonal or brick-wall lattice is of broad interest in material science and of-
 652 ten appears in the context of quantum many-body systems. For instance, the *Kitaev honeycomb*
 653 *model* is a paradigmatic example hosting different kinds of phases supporting different types
 654 of anyons, both Abelian and non-Abelian [107]. We will now describe the general technical
 655 framework to simulate honeycomb lattices with the backbone CTMRG procedure described
 656 in Sec. 2.2. To this end we consider an elementary unit cell of the honeycomb lattice. Here
 657 we choose to define it along so-called x -links for reasons that become clear soon. Alternately
 658 and equivalently, it could as well be defined along y - or z -links. As an example with
 659 eight different tensors on the honeycomb lattice, corresponding to four elementary unit cells
 660 is shown in Fig. 18. Coarse-graining the two lattice sites along x -links of the honeycomb lat-
 661 tice directly results in a square lattice, as shown in Fig. 19. Here, the (mapped) unit cell has
 662 size $(L_x, L_y) = (2, 2)$ with an arrangement as in Eq. (3) and Fig. 1. The green color is used
 663 to highlight the coarse-graining along x -links. In contrast to the regular square lattice, each
 664 coarse-grained tensor has two physical indices that can be reshaped to a single, combined index
 665 before feeding it into the CTMRG procedure. A trivial unit cell on the square lattice, consisting
 666 of only a single-site tensor, results in two different tensors on the honeycomb lattice.

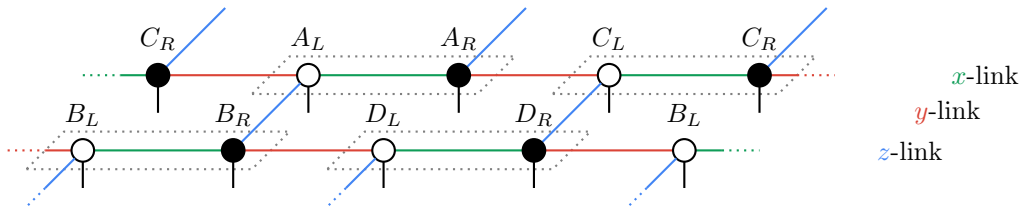


Figure 18: iPEPS ansatz on the honeycomb lattice with four elementary unit cells, resulting in eight different lattice sites. x -, y - and z -links denote the three types of inequivalent links in the lattice. Coarse-graining this state to a square lattice results in a $(L_x, L_y) = (2, 2)$ configuration, with an arrangement as in Eq. (3) / Fig. 1.

667 The CTMRG routine can then be run as described above, just with a larger physical di-
 668 mension. This does not change anything in the contractions, it is just computationally more
 669 expensive. Expectation values can now be evaluated accurately using the CTMRG environ-
 670 ment tensors. Assuming nearest-neighbour terms again, expectation values along x -links can
 671 be computed by a single-site TN, while y - and z -bonds remain two-site TNs similarly to Fig. 11.

672 3.2 Kagome lattice

673 Another important and often encountered lattice in condensed matter physics is the Kagome
 674 lattice. It is of special interest due to its corner-sharing triangles, which lead a strong geomet-
 675 ric frustration for anti-ferromagnetic models. Using a simple mapping of the Kagome lattice
 676 to a square lattice, we can directly incorporate it into our variational PEPS library. The Kagome
 677 lattice is shown in Fig. 20a. Naturally, we can define a unit cell of tensors that is repeated
 678 periodically over the whole two-dimensional lattice. In our setting we consider an upward tri-
 679 angle on the Kagome lattice as an elementary unit cell, highlighted by the gray dotted area in
 680 Fig. 20a. By choosing a coarse-graining, we can represent the three lattice sites in the unit cell
 681 by a single iPEPS tensor, which connects to its neighbours by four virtual indices. This direct
 682 mapping is shown in Fig. 20b. Nearest-neighbour links in the Kagome lattice get mapped to
 683 nearest-neighbour or second-nearest-neighbour links in the square lattice. Every iPEPS site on
 684 the square lattice has a physical dimension of p^3 . As an alternative mapping, which results in
 685 the same coarse-grained TN structure, we move from the Kagome lattice to its dual, the honey-
 686 comb lattice. Here the spins live on the links instead of the vertices. The honeycomb mapping
 687 presented in Sec. 3.1 is therefore not directly applicable and additional simplex tensors are nec-
 688 essary to connect the lattices sites. This TN structure is shown in Fig. 21, which is commonly
 689 known as the infinite *projected entangled simplex state* (iPESS) [108]. Due to this particular
 690 mapping, three Kagome lattice sites (along with two simplex tensors) are coarse-grained into

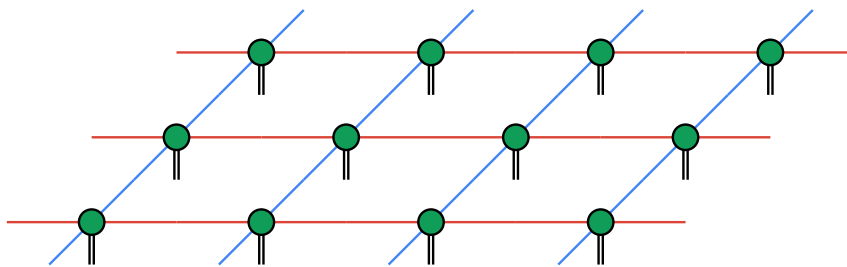


Figure 19: Using a mapping the brick-wall lattice is transformed to the square lattice. The green color of the tensors is just to highlight the coarse-graining along x -links, while y - and z - links remain in the network.

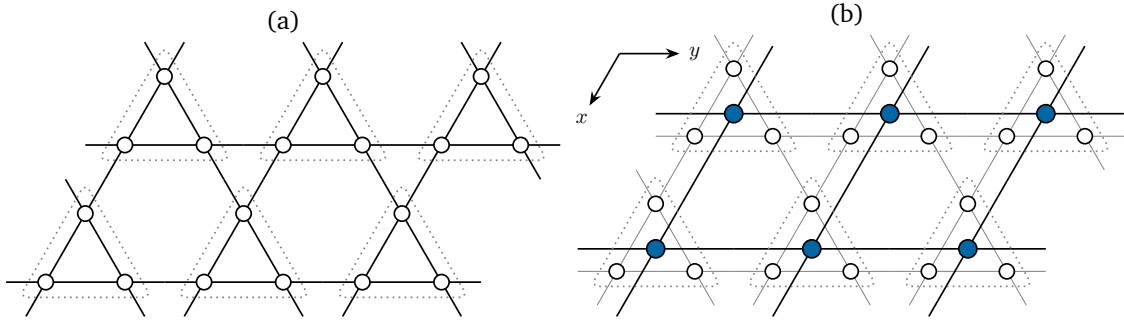


Figure 20: (a) Regular Kagome lattice with corner-sharing triangles and an elementary unit cell consisting of three lattice sites. (b) Regular Kagome lattice mapped to a square lattice by coarse-graining of the three spins in each unit cell.

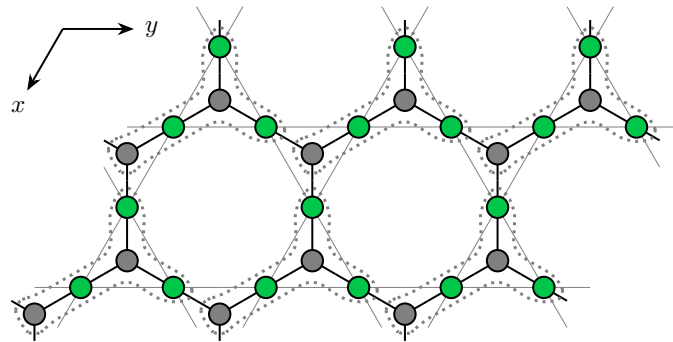


Figure 21: Honeycomb lattice (dual to the Kagome lattice) with spins residing on the lattice links and additional simplex tensors on the lattice sites. Unit cells are highlighted by the gray dotted areas. Upon coarse-graining of the unit cells, the dual honeycomb lattice is mapped to the regular square lattice. Physical indices of the corresponding TN states are not shown.

691 a single iPEPS site on the square lattice. While the mappings in Fig. 20b and Fig. 21 result in
 692 the same square lattice TN, they differ in the number of variational parameters in the ansatz.
 693 In the direct iPEPS ansatz, every unit cell tensor has $p^3 \chi_B^4$ parameters, while there are only
 694 $(3p\chi_B^2 + 2\chi_B^3)$ parameters for the iPES ansatz. Moreover, quantum correlations between lat-
 695 tice sites are exactly captured within the coarse-grained cluster for the iPEPS, whereas they
 696 are limited by the bulk bond dimension for the iPES. In the ladder case, however, there is
 697 no bias between lattice sites within one cluster and sites belonging to different clusters. The
 698 nearest neighbor interactions on the Kagome lattice are mapped to on-site, nearest neighbor
 699 and next-nearest neighbor interactions on the square lattice. As a concrete mapping example
 700 which has particular use in the study of the regular Heisenberg model in a magnetic field, we
 701 consider the iPEPS configuration

$$\mathcal{L} = \begin{pmatrix} A & B & C \\ B & C & A \\ C & A & B \end{pmatrix} \quad (19)$$

702 on the square lattice. This configuration results in the Kagome lattice structure shown in
 703 Fig. 22.

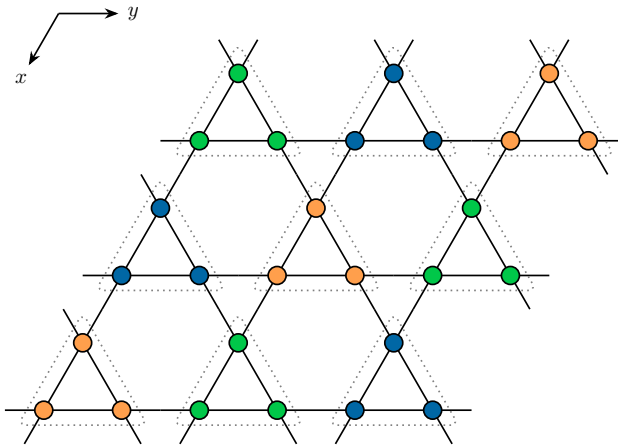


Figure 22: Kagome lattice structure corresponding to a square lattice unit cell according to Eq. (19).

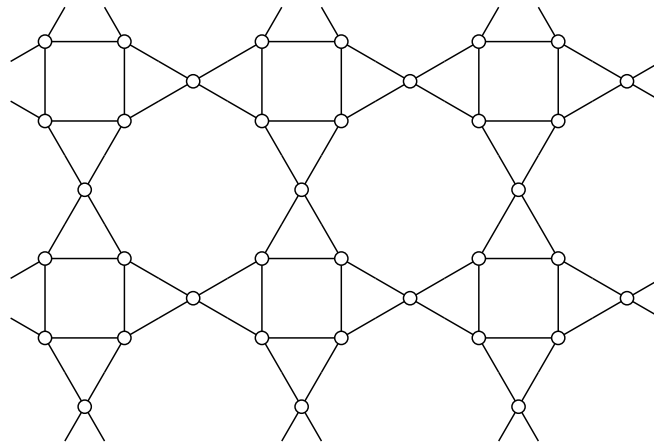


Figure 23: Square-Kagome lattice. Similarly to the regular Kagome lattice, it features corner-sharing triangles. The elementary unit cell consists of six sites, as shown in Fig. 24.

704 3.3 Square-Kagome lattice

705 As a third lattice that has gained a lot of interest in recent time is the square-Kagome lattice.
 706 Similar to the regular Kagome lattice it features corner-sharing triangles and it is expected to
 707 host exotic quantum phases due to the geometric frustration for antiferromagnetic spin models.
 708 The square-Kagome lattice structure is shown in Fig. 23. Naturally, a coarse-graining of the six
 709 spins in the elementary unit cell can be used, which directly maps the square-Kagome lattice
 710 to a square lattice as depicted in Fig. 24. Following the same construction as for the regular
 711 Kagome lattice, we can generalize the iPESS ansatz to the dual of the square-Kagome lattice,
 712 the so-called $(4, 8^2)$ Archimedean lattice. This results in an ansatz with four simplex tensors
 713 and six lattice site tensors per elementary unit cell, as illustrated in Fig. 25. Counting the
 714 number of variational parameters in both TN ansätze, we find a drastic reduction in the iPESS
 715 ansatz, again. Here the iPEPS has $p^6 \chi_B^4$ parameters, while the iPESS only has $(6p\chi_B^2 + 4\chi_B^3)$
 716 parameters for each tensor in the unit cell. In Table 1, we reinforce the difference for usual
 717 iPEPS bond dimensions, which has a strong influence on the expressivity and optimization
 718 of the different TN structures. As in the case of the Kagome lattice, the first coarse-graining
 719 captures quantum correlations within the cluster exactly. While this is not the case for the
 720 iPESS mapping, it does not introduce a bias for the different lattice sites within and across

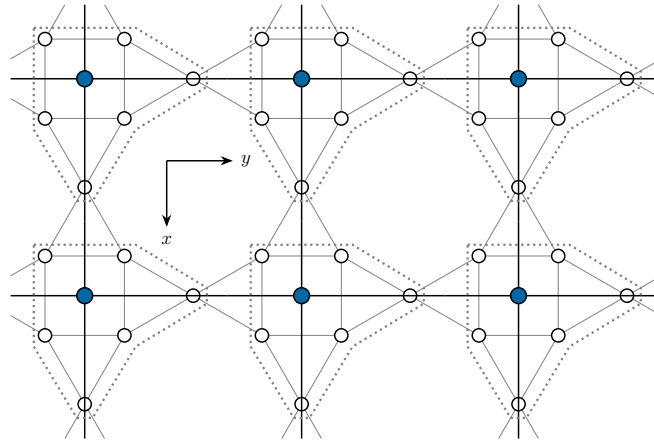


Figure 24: Regular square-Kagome lattice mapped to a square lattice by coarse-graining the six spins in each elementary unit cell.

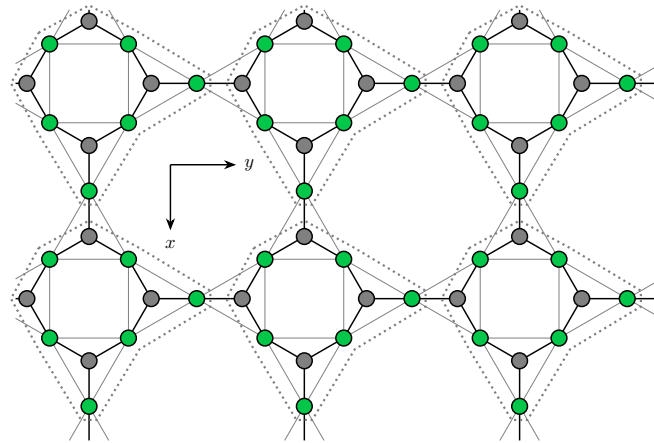


Figure 25: Square-octagon lattice (dual to the square-Kagome lattice) with spins residing on the lattice links and additional simplex tensors on the lattice sites. Unit cells are highlighted by the gray dotted areas. Upon coarse-graining of the unit cells, the square-octagon lattice is mapped to the regular square lattice. Physical indices of the corresponding TN states are not shown.

721 clusters. Both mappings result in a large physical bond dimension of p^6 , with p the Hilbert
 722 space dimension of the original degrees of freedom (e.g., $p = 2$ for a spin-1/2). This makes
 723 especially the CTMRG routine computationally expensive. As an example we consider a two-
 724 site checkerboard pattern $((L_x, L_y) = (2, 2)$ with only two different tensors) on the square
 725 lattice, given by

$$\mathcal{L} = \begin{pmatrix} A & B \\ B & A \end{pmatrix}. \quad (20)$$

726 This results in a square-Kagome state with twelve different lattice sites, as shown in Fig. 26.

727 Assuming nearest-neighbour interactions in the Hamiltonian, the ground state energy can
 728 be computed by single-site as well as horizontal and vertical two-site expectation values.

729 3.4 Triangular lattice

730 The triangular lattice, shown in Fig. 27 is another two-dimensional lattice variant that appears
 731 frequently in condensed matter systems. Due to its large connectivity to six nearest neighbours,

χ_B	$p^6 \chi_B^4$	$(6p\chi_B^2 + 4\chi_B^3)$	ratio
2	1024	80	12.8
3	5184	216	25.0
4	16384	448	36.6
5	40000	800	50.0
6	82944	1296	64.0
7	153664	1960	78.4
8	262144	2816	93.1

Table 1: Number of variational parameters (per elementary unit cell) in the iPEPS and iPESS TN ansatz of the square-Kagome lattice for $p = 2$, assuming real tensor elements.

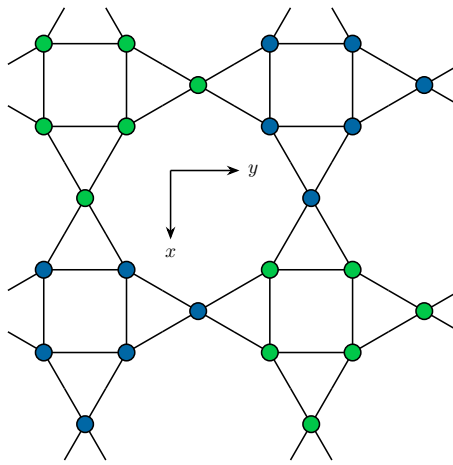


Figure 26: Square-Kagome lattice structure for a square lattice unit cell according to Eq. (20). The ansatz has twelve different lattice sites with two-site translation invariance in both x - and y -direction.

732 it is a typical playground for frustrated systems, hosting a variety of different quantum phases.
 733 As a consequence of this, the large connectivity makes it more challenging for numerical sim-
 734 ulations. The triangular lattice can be directly interpreted as a square lattice with additional
 735 diagonal interactions. The entanglement between diagonal sites is then mediated by the reg-
 736 ular virtual links in the square lattice tensor network. Nearest-neighbour interactions on the
 737 triangular lattice are again mapped to nearest-neighbour and next-to-nearest-neighbour inter-
 738 action on the coarse-grained square lattice.

739 An alternative TN representation of the triangular lattice can be constructed using again
 740 the iPESS ansatz. In contrast to the iPESS for Kagome and square-Kagome lattices, here the
 741 lattice sites have three virtual indices, too. The mapping is visualized in Fig. 28 with the iPESS
 742 ansatz being a honeycomb lattice. Similarly to the first interpretation, this iPESS honeycomb
 743 ansatz can be mapped to a regular square lattice with additional next-to-nearest-neighbour in-
 744 teractions. While the first approach as $p\chi_B^4$ parameters per unit cell tensor, the iPESS mapping
 745 only has $(p\chi_B^3 + \chi_B^3)$ coefficients. Finally, and as an alternative to the previous mappings, a
 746 reverse transformation could be used, which involves a fine-graining of the lattice sites [109].

747 3.5 Comments about different structures

748 In general there is no unique way to map a given lattice structure to the square lattice. The
 749 different approaches mainly differ in the number of variational parameters. While the energy

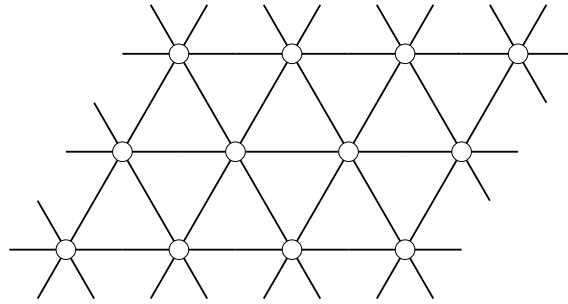


Figure 27: Regular triangular lattice with a connectivity of six, i.e., every lattice site is connected to six nearest neighbours.

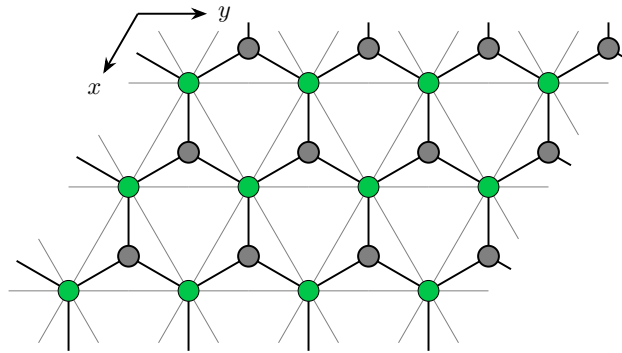


Figure 28: iPESS ansatz for the triangular lattice consisting of only two tensors per triangular lattice site. When one lattice site and one simplex tensor are combined, the triangular lattice is directly mapped onto a regular square lattice.

750 for an ansatz with fewer parameters can be optimized with fewer resources, an ansatz with a
 751 higher variational freedom might be able to capture the physical system more accurately. At
 752 the same time the optimization becomes more complex due to the need to calculate bigger gra-
 753 dients. In practice, choosing the right ansatz depends on the spatial structures of the quantum
 754 state, the amount of entanglement present in the system and the required accuracy. One strat-
 755 egy that works well is a step-wise optimization. In the first step one can choose, e.g., an iPESS
 756 ansatz with fewer variational parameters. Once an optimized wave function has been found,
 757 the iPESS ansatz is coarse-grained into a TN with a higher number of variational parameters,
 758 e.g., a direct iPEPS ansatz. A second optimization of this more expressive ansatz might then
 759 result in lower ground state energies. In the following sections we will present benchmarks,
 760 where several of the lowest data points have been obtained with such a two-step procedure.

761 4 Benchmarks and discussions

762 In this section, we will present benchmarks for a challenging and paradigmatic models on
 763 the different currently supported lattices. Due to its prominence and availability of bench-
 764 marks to different numerical techniques, we generally focus on the spin-1/2 Heisenberg anti-
 765 ferromagnet. The Heisenberg Hamiltonian is given by

$$H = J \sum_{\langle i,j \rangle} \vec{S}_i \cdot \vec{S}_j, \quad (21)$$

766 where $\langle i, j \rangle$ denotes nearest neighbours and \vec{S}_i are the spin-1/2 operators on the lattice sites.
 767 We consider isotropic anti-ferromagnetic interactions at $J = 1.0$ throughout the benchmark

768 section. Variational energies obtained with our implementation are denoted by “*variational*
 769 *update*” (VU). Where applicable, we include different TN variants (e.g., iPESS and iPEPS) in
 770 the numerical benchmarks, to highlight the effect of different numbers of variational param-
 771 eters. Imaginary time-evolution in the form of a “*simple update*” (SU) on the different lattice
 772 structures can provide initial states for the variational update as discussed in Sec. 2.8.3. When-
 773 ever we use initial tensors from the SU, we add a small amount of random noise to the input
 774 tensors prior to the variational update, in order to circumvent possible local minima in the
 775 imaginary time evolution.

776 In the plots of this section we include the energies calculated by the mean-field environ-
 777 ment (MF) used in the simple update. Using this approximation much larger iPEPS bond
 778 dimensions are computationally feasible but we would like to point out that this method is
 779 not guaranteed to be variational in the sense that the energy is an upper bound to the ground
 780 state energy. Thus, it is only sensible to rigorously compare results for which energy expecta-
 781 tion values are computed by CTMRG. We include the non-variational MF energies for higher
 782 iPEPS bond dimensions for a rough comparison.

783 We add for each benchmark a table with the comparison of the results obtained by the
 784 simple update simulations and the best result throughout all variational updates for a fixed
 785 iPEPS bond dimension χ_B . Both expectation values have been calculated by CTMRG.

786 4.1 Comments on lower bounds in variational principles

787 As a further conceptual point, it is important to stress that variational principles can be bench-
 788 marked as well by resorting to lower bounds to ground state energies. Such lower bounds can
 789 be efficiently computed and hold in the thermodynamic limit up to a small constant error in
 790 the energy density [110]. If the Hamiltonian H is seen as being written as a sum of terms

$$H = \sum_j h_j \quad (22)$$

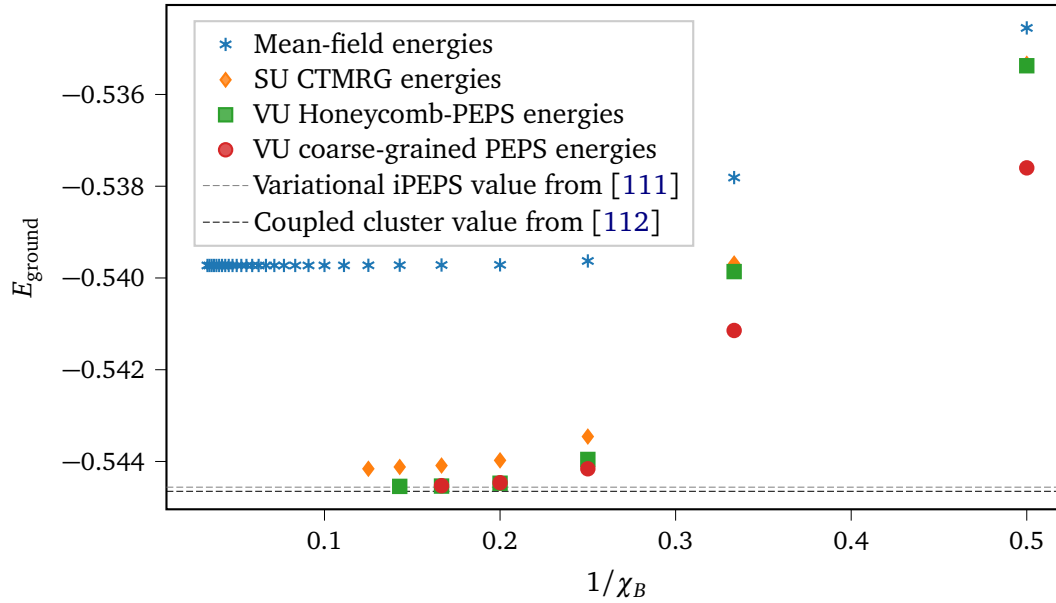
791 where each h_j is a patch that contains as many unit cells that can be accommodated in an
 792 exact diagonalization, then

$$\frac{\langle \psi | H | \psi \rangle}{\langle \psi | \psi \rangle} \geq E_0 \quad \forall |\psi\rangle, \quad E_0 \geq \lambda_{\min}(h_j), \quad (23)$$

793 where $\lambda_{\min}(h_j)$ denotes the smallest eigenvalue of the patch h_j with open boundary conditions.
 794 In this way, the quality of the variational principle giving rise to upper bounds to the ground
 795 state energy can be certified by lower bounds.

796 4.2 Honeycomb lattice

797 For the simulations of the Heisenberg on the honeycomb lattice we choose a single-site unit cell,
 798 consisting of only two different tensors on the honeycomb lattice. A mapping to the square lat-
 799 tice yields a fully translationally invariant iPEPS with a local Hilbert space dimension of $p^2 = 4$.
 800 We optimize the ground states on both TN structures with $2p\chi_B^3$ and $p^2\chi_B^4$ numbers of varia-
 801 tional parameters, respectively (assuming real tensor coefficients). The model is known to be
 802 in a gapless Néel ordered phase [113–115]. Therefore, high environment bond dimensions χ_E
 803 are required to capture the large correlation lengths of the critical state. Ground state energies
 804 are reported in Fig. 29. The critical property of the ground state is already nice reflected in the
 805 significant difference between simple update MF and CTMRG expectation values. The CTMRG
 806 environments treat quantum correlations much more carefully, which leads to improved en-
 807 ergies for the infinite TN state. The VU provides lower energies than the SU with CTMRG



χ_B	E_0 (SU)	E_0 (VU)
2	-0.53533	-0.537600
3	-0.53969	-0.541145
4	-0.54346	-0.544159
5	-0.54398	-0.544474
6	-0.54409	-0.544536
7	-0.54412	-0.544543

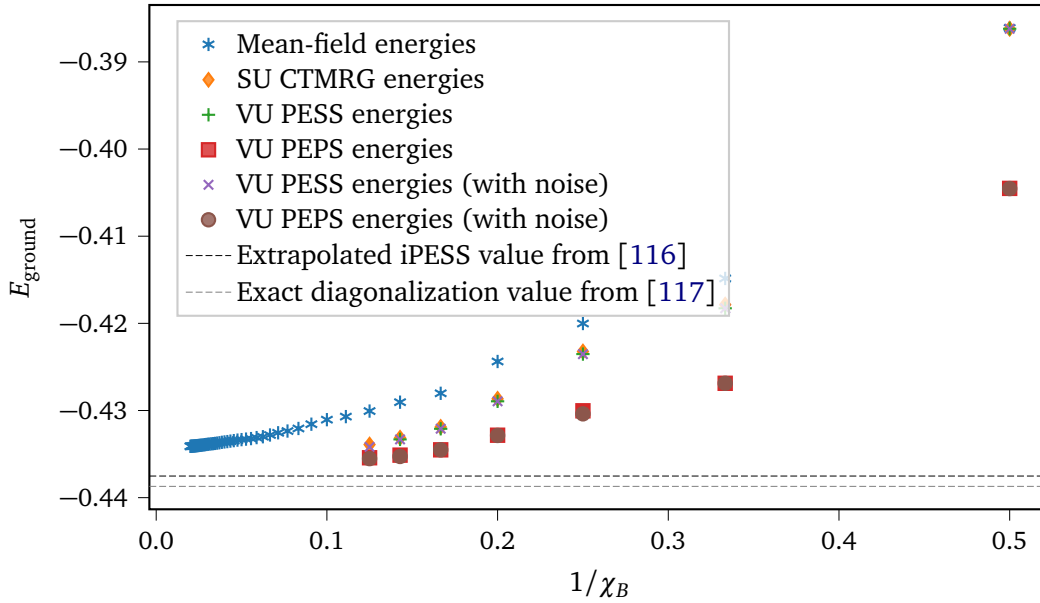
Figure 29: Benchmarking results for the isotropic spin-1/2 Heisenberg model on the honeycomb lattice. For comparison we include the variational result obtained by an iPEPS study in Ref. [111]. Additionally, the result calculated by the coupled cluster method in Ref. [112] is shown, which is due to extrapolation not variational either.

808 and our results using the VU are compatible with previous results using variational iPEPS with
 809 a different CTMRG procedure [111] as well as extrapolated and thus non-variational results
 810 from the coupled cluster method [112].

811 4.3 Kagome lattice

812 The Heisenberg model on the Kagome lattice can be considered one of the most enigmatic and
 813 well studied models in the field of frustrated magnetism [117]. While a spin liquid ground
 814 state is well established, the actual type of ground state is still under debate with different
 815 methods supporting different states (e.g., \mathbb{Z}_2 gapped spin liquid [118, 119], $U(1)$ gapless spin
 816 liquid [116, 120]).

817 Since the ground state is known to be a spin liquid state, that does not form any magnetic
 818 ordering down to zero temperature while preserving lattice translation and rotation symmetry,
 819 we use the smallest unit cells of only three sites in our simulations. The SU then works on the
 820 three-site iPESS ansatz. The VU is performed both on the honeycomb iPESS and on a coarse-
 821 grained, fully translationally invariant iPEPS state. The number of variational parameters are
 822 hence $(3p\chi_B^2 + 2\chi_B^3)$ for the iPESS and $p^3\chi_B^4$ for the iPEPS. Again, the iPEPS state is more
 823 expressive and produces lower variational energies, that follow a smoother convergence with
 824 bond dimension χ_B , see Fig. 30. The ED energy provides a lower-bound for the energy, as
 825 argued in Sec. 4.1. Our energies are compatible with other state-of-the-art numerical methods



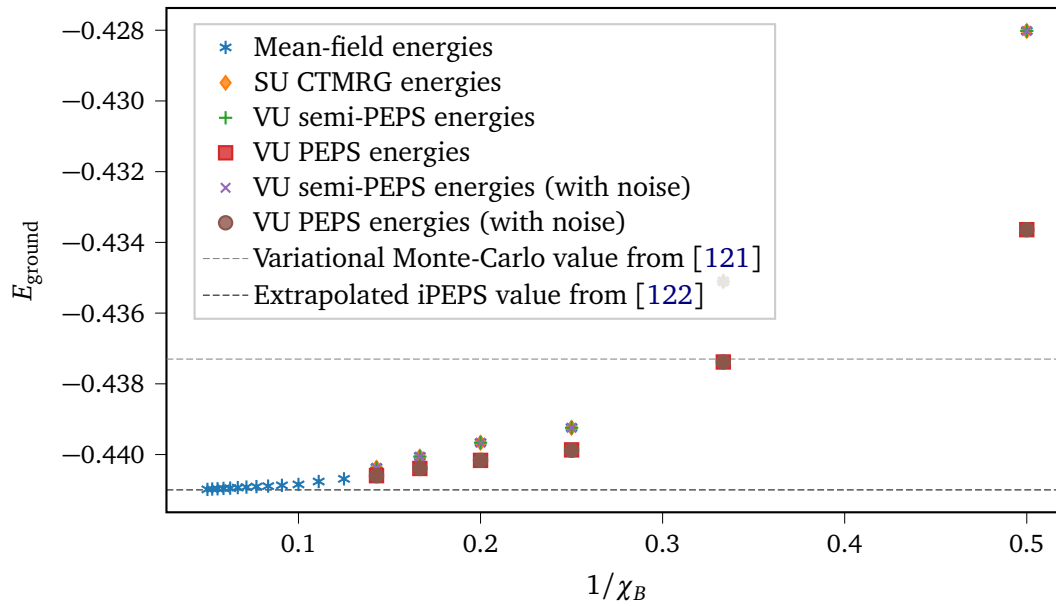
χ_B	E_0 (SU)	E_0 (VU)
2	-0.38620	-0.40454
3	-0.41786	-0.42688
4	-0.42323	-0.43038
5	-0.42866	-0.43286
6	-0.43188	-0.43451
7	-0.43313	-0.43527
8	-0.43391	-0.43552

Figure 30: Benchmarking results for the isotropic spin-1/2 Heisenberg model on the Kagome lattice. For comparison, we show the outcome obtained by extrapolated iPES results in Ref. [116], which, to be strict, is not variational as the authors noted. Additionally, we include the result computed by exact diagonalization in Ref. [117].

826 as the extrapolated iPES result from Ref. [116], but we would like to point out that the authors
 827 noted that their results are not variational and hence the comparison is slightly tainted. Our
 828 result showcases the purpose of variational iPES optimization for highly frustrated systems
 829 to obtain a real upper bound to the ground state energy.

830 4.4 Square-Kagome lattice

831 As a third benchmark model, we simulate the Heisenberg model on the square-Kagome lattice,
 832 a lattice that has gained attention as a class of promising quantum spin liquid materials [123].
 833 It consists of corner-sharing triangles, that generate a high geometric frustration similar to the
 834 Kagome lattice. Its ground state has been found to be non-magnetic, however the existing
 835 subtle competition between different types of *valence bond crystal* (VBC) states has only been
 836 resolved recently in a TN study [122], in favor of a VBC with loop-six resonances. Simulations
 837 of the model are performed for a twelve-site checkerboard unit cell, as shown in Fig. 26.
 838 Results for the ground state energy are presented in Fig. 31. Due to the VBC ground state
 839 with a small correlation length and an energy gap in the model, the simple update MF and
 840 CTMRG energies are nearly identical. The variational update is performed on a so-called semi-
 841 PEPS structure as described in Ref. [122] and also on a coarse-grained iPES TN as introduced
 842 in Fig. 24, a structure that is unfeasible for SU simulations due to the large imaginary time



χ_B	E_0 (SU)	E_0 (VU)
2	-0.42802	-0.43364
3	-0.43511	-0.43738
4	-0.43924	-0.43988
5	-0.43967	-0.44017
6	-0.44006	-0.44039
7	-0.44038	-0.44060

Figure 31: Benchmarking results for the isotropic spin-1/2 Heisenberg model on the square-Kagome lattice. For comparison, we include the variational Monte-Carlo results presented in Ref. [121]. Additionally, we show the extrapolated iPEPS result obtained in Ref. [122], which, to be strict, is not variational. We stress that the mean-field energies also are not variational as discussed in Sec. 4.

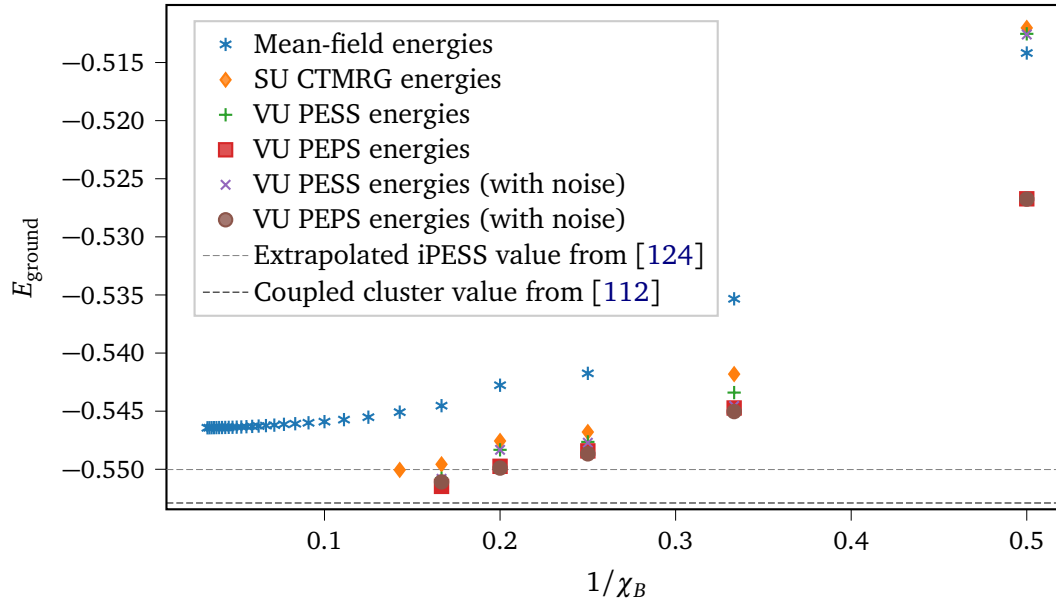
843 evolution operators. Although the VU cannot significantly improve the ground state energy for
 844 the semi-PEPS ansatz, the VU on the full coarse-grained iPEPS structure improves the energies
 845 at the same bond dimension χ_B . This is connected to the larger expressivity of the coarse-
 846 grained structure.

847 Our results outperform variational Monte-Carlo simulations in Ref. [121] and are compa-
 848 rable to state-of-the-art iPEPS results in Ref. [122]. We emphasize that the latter result is in
 849 the extrapolation, strictly speaking, not variational so that a comparison is slightly tainted.

850 4.5 Triangular lattice

851 As a last benchmark model we consider the Heisenberg model on the triangular lattice. Due to
 852 its connectivity of six, the triangular lattice exhibits a large amount of geometric frustration.
 853 The ground state is believed to be a three-sublattice 120° magnetically ordered state [125,
 854 126]. The ground state of the Heisenberg model on the triangular lattice is computed using
 855 a three-sublattice unit cell arranged in an ABC-BCA-CAB structure. The simple update data
 856 has been produced by an iPESS ansatz with the simplices sitting in the upward triangles (see
 857 Fig. 28). The VU is performed in two steps, using the converged iPESS state as input for second
 858 coarse-grained optimization run.

859 The results of our benchmark are shown in Fig. 32. In the case of the triangular lattice



χ_B	E_0 (SU)	E_0 (VU)
2	-0.51202	-0.52675
3	-0.54181	-0.54503
4	-0.54679	-0.54867
5	-0.54756	-0.54990
6	-0.54957	-0.55147

Figure 32: Benchmarking results for the isotropic spin-1/2 Heisenberg model on the triangular lattice with an $ABC - BCA - CAB$ 3×3 unit cell structure. For comparison, we include the extrapolated, thus non-variational coupled cluster results presented in Ref. [112]. Additionally, we show the extrapolated iPESS result obtained in Ref. [124], which, to be strict, is not variational.

860 it generally helps to add some noise on the SU input state to reach better ground states and
 861 energies. We compare against a recent iPESS study based on the simple update [124], that
 862 predicts a zero-temperature magnetisation consistent with previous Monte Carlo studies [127]
 863 and additionally against a result obtained by the extrapolated, thus non-variational coupled
 864 cluster method [112]. We would like to point out that the iPESS result was extrapolated and
 865 is, strictly speaking, not variational.

866 4.6 Comments on excited states

867 In this work, we have primarily focused on providing a comprehensive discussion of the use of
 868 AD for the study of ground state properties of interacting quantum lattice models. It should go
 869 without saying, however, that excited states can be included in a straightforward manner. The
 870 study of excited states has first been initiated in the realm of matrix product states [128], but
 871 has later been generalized to iPEPS [129–131], allowing for constructing variational ansatzes
 872 for elementary excitations on PEPS ground states that facilitate computing gaps, dispersion
 873 relations, and spectral weights in the thermodynamic limit.

874 More recently, automatic differentiation has also found its way into the optimisation of ex-
 875 cited states [42]. The central idea is to construct the excited state with momentum $\vec{k} = (k_x, k_y)$
 876 as a superposition of the ground state vector, perturbed by a single tensor B at position $\vec{x} = (x, y)$

877 and appropriate phase factors according to

$$|\phi(B)_{\vec{k}}\rangle = \sum_{\vec{x}} e^{i\vec{k}\vec{x}} |\phi(B)_{\vec{x}}\rangle. \quad (24)$$

878 The coefficients of tensor B are then determined by energy minimisation of the excited state,
 879 for which AD can again be used [42, 132]. In contrast to the regular ground state optimisation,
 880 here the CTMRG routine must be extended to include the appropriate phase factors in the
 881 directional absorption. Moreover, instead of only eight environment tensors per iPEPS tensor
 882 in the unit cell, the action of B , B^\dagger and the product of B and B^\dagger has to be tracked in three
 883 additional sets of eight tensors.

884 The excited state approach can be directly extended to different lattice geometries. To
 885 this end, we have to generalize the absorption of iPEPS tensors (growing the CTMRG transfer
 886 tensors T_1 , T_2 , T_3 and T_4) to include the basis of the lattice, respecting relative phase factors
 887 of the basis vectors. Depending on the actual structure of the basis, a separate tensor B_n is
 888 chosen as a perturbation for each of the basis site. Our implementation already contains the
 889 main building blocks of a robust and flexible CTMRG routine, calculation of gradients using AD
 890 at the fixed-point and minimisation of an energy cost function. The extension of the framework
 891 to include excited states is therefore natural. It is planned as a future feature.

892 4.7 Comments on fermionic systems

893 As a final comment we stress that for clarity and to be concise, we have focused in our pre-
 894 sentation on quantum spin models. It should be clear, however, that the machinery developed
 895 here readily carries over to the study of *interacting fermionic systems*, with little modifications.
 896 Naively, one might think that the simulation of two-dimensional fermionic models is marred
 897 by substantial overheads that emerge when invoking a spin-to-fermion mapping. This is, how-
 898 ever, not the case, and the respective book-keeping of the signs can be done with negligible
 899 overhead [133, 134]. On the formal level, such tensor networks involve a particular choice
 900 of what is called a spin structure [135, 136]. Practically speaking, one can modify much of
 901 the bosonic code for PEPS to the fermionic setting, readily incorporating the relevant signs
 902 to capture interacting fermions, in what is called *fermionic PEPS* [133, 137, 138]. This insight
 903 is important as some of the most compelling test cases of interacting quantum many-body
 904 systems are of a fermionic nature.

905 5 Conclusion and prospects

906 In this review we present a comprehensive introduction into automatic differentiation in the
 907 context of two-dimensional tensor networks, leading to the recently emerging variational
 908 iPEPS framework for ground state optimization. We provide implementation details and dis-
 909 cuss obstacles that arise in practice, as well as techniques to mitigate these. At the same time,
 910 we coherently present ideas that have to date only been mentioned in a fragmented fashion
 911 in the literature. We hope that the present work can serve as a useful reference and review in
 912 the variational study of 2d tensor networks.

913 This work accompanies the variational iPEPS library *variPEPS*, a comprehensive and ver-
 914 satile code base for optimizing iPEPS in a general setting. We expect this library to be a helpful
 915 tool for performing state-of-the-art tensor network analyses for a wide range of physical mod-
 916 els, featuring multiple two-dimensional lattices. The library is designed to be extended with
 917 additional simulation techniques based on automatic differentiation, such as excited states and
 918 structure factors.

919 The *variPEPS* library is publicly available in both a Julia and a Python version on GitHub [56],
 920 with stable references in the corresponding Zenodo repositories [57, 58].

921 5.1 CO₂-emissions table

922 For the sake of completeness and for promoting carbon footprint awareness, we display an
 923 estimated lower bound of the carbon emissions generated during the course of this work in
 924 Table 2.

Numerical simulations	
Total Kernel Hours [h]	≥ 255276
Thermal Design Power Per Kernel [W]	12
Total Energy Consumption Simulations [kWh]	≥ 3063
Average Emission Of CO ₂ In Germany [kg/kWh]	0.441
Total CO ₂ -Emission For Numerical Simulations [kg]	≥ 1351
Were The Emissions Offset?	Yes
Air Travel	
Total CO ₂ -Emission For Air Travel [kg]	924
Were The Emissions Offset?	Yes
Total CO ₂ -Emission [kg]	≥ 2275

Table 2: Summary of the estimated lower bound of the carbon cost generated during the development of this work. The estimations have been calculated using the examples of the Scientific CO₂nduct project [139] and include the costs of the numerical calculations and air travel for collaborations.

925 Acknowledgements

926 We acknowledge inspiring discussions with Ji-Yao Chen, Andreas Haller, Juraj Hasik, August-
 927 tine Kshetrimayum, Alexander Nietner and Niklas Tausendpfund. We would like to particu-
 928 larly thank Boris Ponsioen, who has for shared valuable insights, and Frederik Wilde, who has
 929 helped us to get the details of the automatic differentiation and the custom fixed-point deriva-
 930 tive correct. We would like to thank the ZEDV (IT support) of the physics department, Freie
 931 Universität Berlin, for computing time and their technical support, particularly we thank Jörg
 932 Behrmann and Jens Dreger.

933 For the Python version we thank the developers of the JAX framework [140, 141] for their
 934 work to provide an AD framework with optimized numerical operations and their technical
 935 support during the development of this work. We also acknowledge the use of the TensorKit
 936 package [91] in the Julia version of the code and wish to advertise the open source libraries
 937 of the Quantum Ghent group in this context [142]. We make use of the Zygote [143] package
 938 for AD in the Julia programming language.

939 The work has been discussed and refined during the workshop “Tensor Networks: Math-
 940 ematical Structures and Novel Algorithms (2022)” at the Erwin Schrödinger International In-
 941 stitute for Mathematics and Physics in Vienna and the workshop “Entanglement in Strongly
 942 Correlated Systems (2023)” at the Centro de Ciencias de Benasque Pedro Pascual. We thank
 943 the organizers for their hospitality and work.

944 **Funding information** E. L. W. thanks the Studienstiftung des deutschen Volkes for support.
 945 This work has been funded by the Deutsche Forschungsgemeinschaft (DFG, German Research

946 Foundation) under the project number 277101999 – CRC 183 (project B01), for which this con-
947 stitutes an inter-node publication involving both Cologne and Berlin, and the BMBF (MUNIQC-
948 Atoms, FermiQP). It has also received funding from the Cluster of Excellence MATH+ and from
949 the Quantum Flagship (PasQuans2).

950 The authors gratefully acknowledge the Gauss Centre for Supercomputing e.V. (www.gauss-
951 centre.eu) for funding this project by providing computing time through the John von Neu-
952 mann Institute for Computing (NIC) on the GCS Supercomputer JUWELS at the Jülich Su-
953 percomputing Centre (JSC) (Grant NeTeNeSyQuMa) and the FZ Jülich for JURECA (institute
954 project PGI-8) [[144](#)].

955 Appendix: Background on automatic differentiation

956 A Adjoint functions and variables

957 In the literature it is common to use so called *adjoint functions* and *adjoint variables* when
 958 using backwards-mode AD. These adjoint functions map the adjoint variables onto each other,
 959 as in Eq. (15) when building up the gradient. In this section, we will briefly introduce the
 960 basic notation of adjoint functions and variables following Ref. [145]. Explicit constructions
 961 of adjoint functions, which are vector-Jacobian-products in the practical implementation, for
 962 a large number of useful operations including those for the iPEPS use-case can be found in
 963 Refs. [145–147].

964 As an example throughout this section, we consider the function h , composed out of two
 965 primitive functions h_1 and h_2 which are concatenated as

$$\begin{aligned} h &= h_2 \circ h_1, \\ h_1 &: M_{n \times n} \times M_{n \times n} \rightarrow M_{n \times n}, \\ h_2 &: M_{n \times n} \rightarrow \mathbb{R}, \end{aligned} \quad (\text{A.1})$$

966 with variables $(A, B) \in M_{n \times n} \times M_{n \times n}$, $C \in M_{n \times n}$ and $x \in \mathbb{R}$. We start by examining the differ-
 967 ential of the output variable x

$$dx = \frac{\partial h_2}{\partial C} dC =: \sum_{i,j} \bar{C}_{i,j} dC_{i,j} = \text{Tr}(\bar{C}^\top dC). \quad (\text{A.2})$$

968 In the first equation, we have suppressed the sum over the indices of C . Eq. (A.2) defines the
 969 adjoint variable \bar{C} of C . We see that the adjoint variable \bar{C} is the derivative of the scalar output
 970 of the function h_2 w.r.t. C . Thus, for the case of a scalar output the variable C and the adjoint
 971 variable \bar{C} have the same dimension. Now, in order to get the gradient ∇h we are interested
 972 in the derivative of the output w.r.t. the input variables (A, B) . To this end we consider the
 973 differential of the intermediate variable

$$dC = \frac{\partial h_1}{\partial A} dA + \frac{\partial h_1}{\partial B} dB. \quad (\text{A.3})$$

974 Inserting this into Eq. (A.2), we obtain

$$dx = \text{Tr} \left(\underbrace{\bar{C}^\top \frac{\partial h_1}{\partial A}}_{\bar{A}^\top} dA \right) + \text{Tr} \left(\underbrace{\bar{C}^\top \frac{\partial h_1}{\partial B}}_{\bar{B}^\top} dB \right). \quad (\text{A.4})$$

975 Here we have already implicitly used the adjoint function \bar{h}_1 that maps the adjoint variable \bar{C}
 976 to the adjoint variables \bar{A} and \bar{B} according to

$$\bar{h}_1 : \bar{C}^\top \mapsto (\bar{A}^\top, \bar{B}^\top)^\top = \left(\bar{C}^\top \frac{\partial h_1}{\partial A}, \bar{C}^\top \frac{\partial h_1}{\partial B} \right)^\top. \quad (\text{A.5})$$

977 Given the fact that we are dealing with a scalar output variable x , we recall that \bar{C} can be
 978 considered a vector, such that the adjoint function is a vector-Jacobian-product (vJP). We can
 979 see that the this mapping of the adjoint variables with adjoint functions eventually produces
 980 the gradient

$$\begin{aligned} \nabla h &= (\bar{A}, \bar{B}) = \left(\frac{\partial h_1}{\partial A} \bar{C}, \frac{\partial h_1}{\partial B} \bar{C} \right) \\ &= \left(\frac{\partial h_1}{\partial A} \frac{\partial h_2}{\partial C}, \frac{\partial h_1}{\partial B} \frac{\partial h_2}{\partial C} \right). \end{aligned} \quad (\text{A.6})$$

981 B Automatic differentiation for complex variables

982 Some extra attention has to be given to the case in which the primitive functions are complex
 983 valued. This is because not all functions one might want to consider are complex-differentiable
 984 (holomorphic) and as such the derivative depends on the direction we move in the complex
 985 plane when taking the limit for the derivative. In such a case one needs to resort to the calculus
 986 of two sets of independent real variables. For a generic function $f : \mathbb{C} \rightarrow \mathbb{C}$ this can be done
 987 by treating x and y in $z = x + iy$ as independent variables or alternatively, by choosing z
 988 and z^* and making use of Wirtinger calculus. However we should also note that in the iPEPS
 989 use case we deal with a function $E : \mathbb{C}^n \rightarrow \mathbb{R}$, which removes the necessity to think about
 990 holomorphism.

991 C The implicit function theorem and its use at the CTMRG fixed- 992 point

993 In this section, we are going to present an alternative approach to taking the derivative of the
 994 energy function by utilizing the fixed point of the CTMRG procedure. To this end, we can
 995 make use of the implicit function theorem [148] to calculate the derivative of the full fixed-
 996 point routine. Our discussion will follow the description of Refs. [149, 150]. Differentiating
 997 Eq. (16) on both sides we end up with

$$\partial_A e^*(A) = \partial_A c(A, e^*) + \partial_{e^*} c(A, e^*) \partial_A e^*(A). \quad (\text{C.1})$$

998 Introducing the shorthand writing for the Jacobians $L = \partial_A c(A, e^*(A))$ and $K = \partial_{e^*} c(A, e^*(A))$
 999 and rearranging the equation we find

$$\begin{aligned} \partial_A e^*(A) &= (L + K \partial_A e^*(A)) \\ &= \left(\sum_{n=0}^{\infty} K^n \right) L = (\mathbb{1} - K)^{-1} L. \end{aligned} \quad (\text{C.2})$$

1000 As discussed in Appendix A, we aim at finding the adjoint function of the CTMRG iteration at
 1001 the fixed point, which is a *vector-Jacobian product* (vJP) $\mathbf{v}^\top \partial_A e^*(A)$. Inserting Eq. (C.2) yields

$$\mathbf{v}^\top \partial e^*(A) = \mathbf{v}^\top (\mathbb{1} - K)^{-1} L = \mathbf{w}^\top L, \quad (\text{C.3})$$

1002 where we have introduced $\mathbf{w}^\top := \mathbf{v}^\top (\mathbb{1} - K)^{-1}$. The second equality in the equation above can
 1003 be rearranged into another fixed-point equation

$$\mathbf{w}^\top = \mathbf{v}^\top + \mathbf{w}^\top K. \quad (\text{C.4})$$

1004 Here $\mathbf{w}^\top K$ is another vJP but this time only dependent of the derivative of a single absorption
 1005 step evaluated at the fixed-point of the CTMRG routine. Solving Eq. (C.4) we can find \mathbf{w}^\top
 1006 to calculate the vJP of the CTMRG routine from Eq. (C.3). In the end we reduced the naive
 1007 effort of unrolling the fixed-point iterations to just calculate the derivative of a single CTMRG
 1008 iteration and another fixed-point iteration which both are much less memory intensive.

1009 D Automatic differentiation in the language of differential geom- 1010 etry

1011 In order to unify the different frameworks for thinking about forward- and backwards-mode
 1012 AD, we will briefly introduce a mathematical notation for AD. It also serves to give some

1013 more precise meaning to the terms “push-forward” and “pullback”, that are sometimes used in
 1014 forward- and backwards-mode AD discussions, respectively. For this we first recall the general
 1015 concept of a push-forward and a pullback for the simple case of functions and distributions.
 1016 Imagine two functions $f : M \rightarrow N$ and $g : N \rightarrow \mathbb{R}$. The *pullback* of g along f allows us to
 1017 construct a function $f^*g : M \rightarrow \mathbb{R}$ for which the domain of the function g is “pulled back” to
 1018 the domain of the function f . This is done by a simple concatenation of f and g

$$f^*g(\underbrace{m}_{\in M}) = (g \circ f)(m) = g(f(m)). \tag{D.1}$$

1019 This construction can now be used to define a *push-forward* on the dual objects of the functions
 1020 under integration. These dual objects are distributions. With a distribution, we can integrate
 1021 a function

$$\int_M \bullet \mu : \mathcal{F}(M) \rightarrow \mathbb{R}, \tag{D.2}$$

$$f \mapsto \int_M f \mu,$$

1022 where $\mathcal{F}(M)$ are just the functions on M and μ is the distribution. Given such a distribution
 1023 on M we can now integrate functions on M . The push-forward $f_*\mu$ of μ allows us to integrate
 1024 functions on N by defining a distribution that is “pushed forward” to N . This works as

$$\int_N h(f_*\mu) =: \int_M (f^*h)\mu, \tag{D.3}$$

1025 where h is a function on N .

1026 This type of construction for the pullback and push-forward generalizes to many mathe-
 1027 matical objects that have a *pairing dual*. The relevant mathematical objects for AD are the
 1028 derivative $\partial/\partial x_i$ and its pairing dual, the differential dx_i .

1029 It might be useful, beyond the conceptual clarity of this notation, to look at AD in this
 1030 way because one can easily imagine situations where the intermediate data of a function is
 1031 restricted by constraints such that the “data-space” becomes geometrically non-trivial. An
 1032 example could be vectors in \mathbb{R}^n restricted to unit length or matrices in $M_{n,m}$ restricted to be
 1033 unitary. We note that an optimisation in these situations requires some additional concepts,
 1034 like finding a path on the given space from a tangent vector. This requires some extra care and
 1035 is not discussed here.

We now introduce the mathematical notation that we need in order to talk about AD in
 this language. We will not be particularly rigorous in this endeavour and leave out all details
 that are not explicitly needed. We start with a manifold M on which we can consider points
 $p \in M$, as well as functions $f : M \rightarrow \mathbb{R}$. For each point $p \in M$ we can define a vector space
 T_pM (call it the tangent-space at p) of tangent-vectors at that point. The elements in T_pM act
 like derivatives on functions on M

$$\text{e.g.: } \frac{\partial}{\partial x_i} = e_i \in T_pM, \quad \frac{\partial}{\partial x_i}(f) = \frac{\partial f}{\partial x_i}.$$

Here we have assumed that we have equipped the manifold M with coordinates via a chart
 $\phi : M \rightarrow \mathbb{R}^m$ around the point p , where $m = \dim(M)$. Our tangent-space T_pM has dimension
 m and we can choose a canonical basis

$$\left\{ \frac{\partial}{\partial x_1}, \dots, \frac{\partial}{\partial x_m} \right\} = \{e_1, \dots, e_m\}.$$

One further defines the dual vector space T_p^*M of the tangent vector space, called cotangent-space. This cotangent-space contains the dual vectors to the derivatives $\frac{\partial}{\partial x_i}$. These cotangent vectors from the cotangent-space are the differentials dx_i . The cotangent-space also has dimension m and we can choose the canonical basis

$$\{dx_1, \dots, dx_m\}.$$

1036 Obviously, given the canonical basis for the tangent-space and cotangent-space we can expand
1037 arbitrary vectors in these spaces in the basis. Take $v \in T_pM$ and $df \in T_p^*M$ we can expand as

$$v = \sum_i v_i \frac{\partial}{\partial x_i} = \sum_i v_i e_i, \quad (\text{D.4})$$

$$df = \sum_i \frac{\partial f}{\partial x_i} dx_i. \quad (\text{D.5})$$

1038 We have a pairing between the derivatives that live in the tangent-space T_pM and the differ-
1039 entials that live in T_p^*M as

$$dx_j \left(\frac{\partial}{\partial x_i} \right) := \frac{\partial x_j}{\partial x_i} = \delta_{i,j}. \quad (\text{D.6})$$

1040 Note that by this pairing relation we see that tangent and cotangent vectors are “pairing duals”
1041 and we can use an analogous construction for pullbacks and push-forwards as we did for
1042 functions and distribution above. Since T_pM and T_p^*M are isomorphic, we can introduce a
1043 correspondence transformation between the canonical basis of the two spaces

$$\bullet^b : T_pM \rightarrow T_p^*M, \quad e_i \mapsto dx_i = e_i^b, \quad (\text{D.7})$$

$$\bullet^\sharp : T_p^*M \rightarrow T_pM, \quad dx_i \mapsto e_i = dx_i^\sharp. \quad (\text{D.8})$$

1044 We now have assembled all necessary tools to formulate what a “gradient” is in this language.
1045 It is given by

$$\nabla f := (df)^\sharp, \quad (\text{D.9})$$

1046 which matches the common formula

$$\begin{aligned} \nabla f &= \left(\sum_i \frac{\partial f}{\partial x_i} dx_i \right)^\sharp = \sum_i \frac{\partial f}{\partial x_i} e_i \\ &= \left(\frac{\partial f}{\partial x_1}, \dots, \frac{\partial f}{\partial x_m} \right), \end{aligned} \quad (\text{D.10})$$

1047 where we have taken e_i just as the i -th unit vector of T_pM .

1048 Now it is easy to construct the pullbacks and push-forwards in this context analogous to our
1049 treatment of functions and distributions. For this we start from manifolds M and N with points
1050 $p \in M$ and $q \in N$, and with the two functions $f : M \rightarrow N$ and $g : N \rightarrow \mathbb{R}$. We can consider a
1051 differential $dg \in T_q^*N$ which we want to “pull back” along the function f and associate it with
1052 and element of $T_{f^{-1}(q)}^*M$, where $f^{-1}(q) \in M$. We do this with the familiar definition

$$\underbrace{f^* dg}_{\in T_{f^{-1}(q)}^*M} := d(g \circ f) \quad (\text{D.11})$$

1053 which uses a concatenation of f and g just as in the first example. For a tangible example
1054 consider $g = x_i$ to be a coordinate function. We then get $f^* dx_i = d(x_i \circ f) = d(f_i)$. As

1055 before the push-forward can be defined via the pullback just as we had done for functions and
 1056 distributions. In this case, we start with a tangent vector $\frac{\partial}{\partial x_i}$ in $T_p M$ and want to “push it
 1057 forward” along f into $T_{f(p)} N$. This works as

$$\underbrace{\left(f_* \left(\frac{\partial}{\partial x_i} \right)\right)}_{\in T_{f(p)} N} (g) := \frac{\partial}{\partial x_i} (f^* g) = \frac{\partial}{\partial x_i} (g \circ f). \quad (\text{D.12})$$

1058 Now that we are equipped with the pullback and push-forward of differentials and derivatives
 1059 we see how the gradient is calculated in the forward- and backward-mode AD. For this we will
 1060 go back to our neat example from Sec. 2.4 and slightly generalize. Say, we would like to take
 1061 the gradient ∇E of a function that is composed of three primitive functions $E = f_3 \circ f_2 \circ f_1$.
 1062 We say these primitive functions map between manifolds

$$E : M_1 \xrightarrow{f_1} M_2 \xrightarrow{f_2} M_3 \xrightarrow{f_3} \mathbb{R}. \quad (\text{D.13})$$

1063 Lets first look at what happens when we build the gradient using backwards-mode AD. In this
 1064 case we start with the differential df_3 of the last primary function of E . This differential lives
 1065 in $T_k^* M_3$, where $k \in M_3$ is a point in M_3 . We can now use the pullback along the functions f_2
 1066 and then f_1 to pull back this differential to M_1

$$f_1^*(f_2^*(df_3)) \xleftarrow{\text{pullback}} f_2^*(df_3) \xleftarrow{\text{pullback}} df_3. \quad (\text{D.14})$$

1067 With the definitions above we see that in this way we construct the gradient

$$f_1^*(f_2^*(df_3)) = f_1^*((d(f_3 \circ f_2))) = d(f_3 \circ f_2 \circ f_1) = dE. \quad (\text{D.15})$$

1068 With our identification between tangent and cotangent vectors we finalize to $\nabla E = (dE)^\sharp$. If
 1069 we express the differential that we start from df_3 in coordinates, we straightforwardly obtain
 1070 the product of Jacobians as a result for the gradient. This also establishes the connection to
 1071 the adjoint functions we talked about in the previous section and the vector-Jacobian product
 1072 as discussed in Sec. 2.4.

1073 In the case of forward-mode AD we start from a tangent vector $\frac{\partial}{\partial x_i}$, which lives in $T_l M_1$,
 1074 where $l \in M_1$ is a point in M_1 . We can now push this tangent vector forward into a tangent
 1075 space of M_3 with successive push-forwards along f_1 followed by f_2

$$\frac{\partial}{\partial x_i} \xrightarrow{\text{push-forward}} f_{1*} \left(\frac{\partial}{\partial x_i} \right) \xrightarrow{\text{push-forward}} f_{2*} \left(f_{1*} \left(\frac{\partial}{\partial x_i} \right) \right). \quad (\text{D.16})$$

1076 With the definitions for the push-forward we see that the gradient we obtain in this way is
 1077 given by

$$\begin{aligned} \sum_i f_{2*} \left(f_{1*} \left(\frac{\partial}{\partial x_i} \right) \right) (f_3) e_i &= \sum_i f_{1*} \left(\frac{\partial}{\partial x_i} \right) (f_3 \circ f_2) e_i \\ &= \sum_i \frac{\partial}{\partial x_i} \underbrace{(f_3 \circ f_2 \circ f_1)}_{=E} e_i \\ &= \nabla E. \end{aligned} \quad (\text{D.17})$$

References

- 1078
- 1079 [1] T. Nishino, *DMRG homepage* (2020), <http://quattro.phys.sci.kobe-u.ac.jp/dmrg/>
1080 [condmat91.html](http://quattro.phys.sci.kobe-u.ac.jp/dmrg/condmat91.html).
- 1081 [2] H. A. Kramers and G. H. Wannier, *Statistics of the two-dimensional ferromagnet. part ii*,
1082 Phys. Rev. **60**, 263 (1941), doi:[10.1103/PhysRev.60.263](https://doi.org/10.1103/PhysRev.60.263).
- 1083 [3] R. Baxter, *Dimers on a rectangular lattice*, J. Math. Phys. **9**, 650–654 (1968),
1084 doi:[10.1063/1.1664623](https://doi.org/10.1063/1.1664623).
- 1085 [4] S. R. White, *Density matrix formulation for quantum renormalization groups*, Phys. Rev.
1086 Lett. **69**, 2863 (1992), doi:[10.1103/PhysRevLett.69.2863](https://doi.org/10.1103/PhysRevLett.69.2863).
- 1087 [5] U. Schollwöck, *The density-matrix renormalization group in the age of matrix product*
1088 *states*, Ann. Phys. **326**, 96 (2011), doi:[10.1016/j.aop.2010.09.012](https://doi.org/10.1016/j.aop.2010.09.012).
- 1089 [6] S. Östlund and S. Rommer, *Thermodynamic limit of density matrix renormalization*,
1090 Phys. Rev. Lett. **75**, 3537 (1995), doi:[10.1103/PhysRevLett.75.3537](https://doi.org/10.1103/PhysRevLett.75.3537).
- 1091 [7] J. Dukelsky, M. A. Martin-Delgado, T. Nishino and G. Sierra, *Equivalence of the vari-*
1092 *ational matrix product method and the density matrix renormalization group applied to*
1093 *spin chains*, Europhys. Lett. **43**, 457 (1998), doi:[10.1209/epl/i1998-00381-x](https://doi.org/10.1209/epl/i1998-00381-x).
- 1094 [8] D. Perez-Garcia, F. Verstraete, M. Wolf and J. Cirac, *Matrix product state representations*,
1095 Quant. Inf. Comp. **7**, 401 (2007), doi:[10.26421/QIC7.5-6-1](https://doi.org/10.26421/QIC7.5-6-1).
- 1096 [9] M. Fannes, B. Nachtergaele and R. Werner, *Finitely correlated states on quantum spin*
1097 *chains*, Commun. Math. Phys. **144**, 443 (1992), doi:[10.1007/BF02099178](https://doi.org/10.1007/BF02099178).
- 1098 [10] C. Lubich, I. V. Oseledets and B. Vandereycken, *Time integration of tensor trains*, SIAM
1099 J. Num. An. **53**(2), 917 (2015), doi:[10.1137/140976546](https://doi.org/10.1137/140976546).
- 1100 [11] R. Orús, *A practical introduction to tensor networks: Matrix product states and projected*
1101 *entangled pair states*, Ann. Phys. **349**, 117 (2014), doi:[10.1016/j.aop.2014.06.013](https://doi.org/10.1016/j.aop.2014.06.013).
- 1102 [12] J. C. Bridgeman and C. T. Chubb, *Hand-waving and interpretive dance: An introduc-*
1103 *tory course on tensor networks*, J. Phys. A **50**, 223001 (2017), doi:[10.1088/1751-](https://doi.org/10.1088/1751-8121/aa6dc3)
1104 [8121/aa6dc3](https://doi.org/10.1088/1751-8121/aa6dc3).
- 1105 [13] J. I. Cirac, D. Pérez-García, N. Schuch and F. Verstraete, *Matrix product states and*
1106 *projected entangled pair states: Concepts, symmetries, theorems*, Rev. Mod. Phys. **93**,
1107 045003 (2021), doi:[10.1103/RevModPhys.93.045003](https://doi.org/10.1103/RevModPhys.93.045003).
- 1108 [14] F. Verstraete, J. I. Cirac and V. Murg, *Matrix product states, projected entangled pair*
1109 *states, and variational renormalization group methods for quantum spin systems*, Adv.
1110 Phys. **57**, 143 (2008), doi:[10.1080/14789940801912366](https://doi.org/10.1080/14789940801912366).
- 1111 [15] J. Eisert, M. Cramer and M. B. Plenio, *Area laws for the entanglement entropy*, Rev. Mod.
1112 Phys. **82**, 277 (2010), doi:[10.1103/RevModPhys.82.277](https://doi.org/10.1103/RevModPhys.82.277).
- 1113 [16] F. Verstraete and J. I. Cirac, *Renormalization algorithms for Quantum-Many Body Systems*
1114 *in two and higher dimensions* (2004), <https://arxiv.org/abs/cond-mat/0407066>.
- 1115 [17] D. Perez-Garcia, F. Verstraete, M. M. Wolf and J. I. Cirac, *PEPS as unique ground states*
1116 *of local Hamiltonians*, Quant. Inf. Comp. **8**, 650 (2008), doi:[10.26421/QIC8.6-7-6](https://doi.org/10.26421/QIC8.6-7-6).

- 1117 [18] N. Schuch, D. Perez-Garcia and I. Cirac, *Classifying quantum phases using matrix*
1118 *product states and projected entangled pair states*, Phys. Rev. B **84**, 165139 (2011),
1119 doi:[10.1103/PhysRevB.84.165139](https://doi.org/10.1103/PhysRevB.84.165139).
- 1120 [19] N. Schuch, M. M. Wolf, F. Verstraete and J. I. Cirac, *Computational com-*
1121 *plexity of projected entangled pair states*, Phys. Rev. Lett. **98**, 140506 (2007),
1122 doi:[10.1103/PhysRevLett.98.140506](https://doi.org/10.1103/PhysRevLett.98.140506).
- 1123 [20] J. Haferkamp, D. Hangleiter, J. Eisert and M. Gluza, *Contracting projected en-*
1124 *tangled pair states is average-case hard*, Phys. Rev. Research **2**, 013010 (2020),
1125 doi:[10.1103/PhysRevResearch.2.013010](https://doi.org/10.1103/PhysRevResearch.2.013010).
- 1126 [21] M. Schwarz, O. Buerschaper and J. Eisert, *Approximating local observ-*
1127 *ables on projected entangled pair states*, Phys. Rev. A **95**, 060102 (2017),
1128 doi:[10.1103/PhysRevA.95.060102](https://doi.org/10.1103/PhysRevA.95.060102).
- 1129 [22] J. Jordan, R. Orús, G. Vidal, F. Verstraete and J. I. Cirac, *Classical simulation of infinite-*
1130 *size quantum lattice systems in two spatial dimensions*, Phys. Rev. Lett. **101**, 250602
1131 (2008), doi:[10.1103/PhysRevLett.101.250602](https://doi.org/10.1103/PhysRevLett.101.250602).
- 1132 [23] H. N. Phien, J. A. Bengua, H. D. Tuan, P. Corboz and R. Orús, *Infinite projected entangled*
1133 *pair states algorithm improved: Fast full update and gauge fixing*, Phys. Rev. B **92**, 035142
1134 (2015), doi:[10.1103/PhysRevB.92.035142](https://doi.org/10.1103/PhysRevB.92.035142).
- 1135 [24] R. Orús and G. Vidal, *Simulation of two-dimensional quantum systems on an infinite*
1136 *lattice revisited: Corner transfer matrix for tensor contraction*, Phys. Rev. B **80**, 094403
1137 (2009), doi:[10.1103/PhysRevB.80.094403](https://doi.org/10.1103/PhysRevB.80.094403).
- 1138 [25] T. Nishino and K. Okunishi, *Corner transfer matrix renormalization group method*, J.
1139 Phys. Soci. Jap, **65**(4), 891 (1996), doi:[10.1143/JPSJ.65.891](https://doi.org/10.1143/JPSJ.65.891).
- 1140 [26] T. Nishino and K. Okunishi, *Corner transfer matrix algorithm for classical renormalization*
1141 *group*, J. Phys. Soc. Jap. **66**(10), 3040 (1997), doi:[10.1143/JPSJ.66.3040](https://doi.org/10.1143/JPSJ.66.3040).
- 1142 [27] M. Levin and C. P. Nave, *Tensor renormalization group approach to two-*
1143 *dimensional classical lattice models*, Phys. Rev. Lett. **99**, 120601 (2007),
1144 doi:[10.1103/PhysRevLett.99.120601](https://doi.org/10.1103/PhysRevLett.99.120601).
- 1145 [28] Z. Y. Xie, H. C. Jiang, Q. N. Chen, Z. Y. Weng and T. Xiang, *Second*
1146 *renormalization of tensor-network states*, Phys. Rev. Lett. **103**, 160601 (2009),
1147 doi:[10.1103/PhysRevLett.103.160601](https://doi.org/10.1103/PhysRevLett.103.160601).
- 1148 [29] H. H. Zhao, Z. Y. Xie, Q. N. Chen, Z. C. Wei, J. W. Cai and T. Xiang,
1149 *Renormalization of tensor-network states*, Phys. Rev. B **81**, 174411 (2010),
1150 doi:[10.1103/PhysRevB.81.174411](https://doi.org/10.1103/PhysRevB.81.174411).
- 1151 [30] Z. Y. Xie, J. Chen, M. P. Qin, J. W. Zhu, L. P. Yang and T. Xiang, *Coarse-graining renormal-*
1152 *ization by higher-order singular value decomposition*, Phys. Rev. B **86**, 045139 (2012),
1153 doi:[10.1103/PhysRevB.86.045139](https://doi.org/10.1103/PhysRevB.86.045139).
- 1154 [31] V. Zauner-Stauber, L. Vanderstraeten, M. T. Fishman, F. Verstraete and J. Haegeman,
1155 *Variational optimization algorithms for uniform matrix product states*, Phys. Rev. B **97**,
1156 045145 (2018), doi:[10.1103/PhysRevB.97.045145](https://doi.org/10.1103/PhysRevB.97.045145).

- 1157 [32] A. Nietner, B. Vanhecke, F. Verstraete, J. Eisert and L. Vanderstraeten, *Efficient varia-*
1158 *tional contraction of two-dimensional tensor networks with a non-trivial unit cell*, *Quan-*
1159 *tum* **4**, 328 (2020), doi:[10.48550/arXiv.2003.01142](https://doi.org/10.48550/arXiv.2003.01142).
- 1160 [33] C. M. Dawson, J. Eisert and T. J. Osborne, *Unifying variational methods for*
1161 *simulating quantum many-body systems*, *Phys. Rev. Lett.* **100**, 130501 (2008),
1162 doi:[10.1103/PhysRevLett.100.130501](https://doi.org/10.1103/PhysRevLett.100.130501).
- 1163 [34] J. Haegeman, J. I. Cirac, T. J. Osborne, I. Pižorn, H. Verschelde and F. Verstraete,
1164 *Time-dependent variational principle for quantum lattices*, *Phys. Rev. Lett.* **107**, 070601
1165 (2011), doi:[10.1103/PhysRevLett.107.070601](https://doi.org/10.1103/PhysRevLett.107.070601).
- 1166 [35] P. Corboz, *Variational optimization with infinite projected entangled-pair states*, *Phys.*
1167 *Rev. B* **94**, 035133 (2016), doi:[10.1103/PhysRevB.94.035133](https://doi.org/10.1103/PhysRevB.94.035133).
- 1168 [36] L. Vanderstraeten, J. Haegeman, P. Corboz and F. Verstraete, *Gradient methods for vari-*
1169 *ational optimization of projected entangled-pair states*, *Phys. Rev. B* **94**, 155123 (2016),
1170 doi:[10.1103/PhysRevB.94.155123](https://doi.org/10.1103/PhysRevB.94.155123).
- 1171 [37] H.-J. Liao, J.-G. Liu, L. Wang and T. Xiang, *Differentiable programming tensor networks*,
1172 *Phys. Rev. X* **9**, 031041 (2019), doi:[10.1103/PhysRevX.9.031041](https://doi.org/10.1103/PhysRevX.9.031041).
- 1173 [38] C. Hubig, *Use and implementation of autodifferentiation in tensor network methods with*
1174 *complex scalars* (2019), <https://arxiv.org/abs/1907.13422>.
- 1175 [39] W.-L. Tu, H.-K. Wu, N. Schuch, N. Kawashima and J.-Y. Chen, *Generating func-*
1176 *tion for tensor network diagrammatic summation*, *Phys. Rev. B* **103**, 205155 (2021),
1177 doi:[10.1103/PhysRevB.103.205155](https://doi.org/10.1103/PhysRevB.103.205155).
- 1178 [40] J. Hasik, D. Poilblanc and F. Becca, *Investigation of the Néel phase of the frustrated*
1179 *Heisenberg antiferromagnet by differentiable symmetric tensor networks*, *SciPost Phys.*
1180 **10**, 012 (2021), doi:[10.21468/SciPostPhys.10.1.012](https://doi.org/10.21468/SciPostPhys.10.1.012).
- 1181 [41] J. Hasik, M. Van Damme, D. Poilblanc and L. Vanderstraeten, *Simulating chiral spin*
1182 *liquids with projected entangled-pair states*, *Phys. Rev. Lett.* **129**, 177201 (2022),
1183 doi:[10.1103/PhysRevLett.129.177201](https://doi.org/10.1103/PhysRevLett.129.177201).
- 1184 [42] B. Ponsioen, F. F. Assaad and P. Corboz, *Automatic differentiation applied to*
1185 *excitations with Projected Entangled Pair States*, *SciPost Phys.* **12**, 6 (2022),
1186 doi:[10.21468/SciPostPhys.12.1.006](https://doi.org/10.21468/SciPostPhys.12.1.006).
- 1187 [43] M. J. O'Rourke and G. K.-L. Chan, *Entanglement in the quantum phases of an unfrustrated*
1188 *rydberg atom array* (2022), <https://arxiv.org/abs/2201.03189>.
- 1189 [44] I. V. Lukin and A. G. Sotnikov, *Variational optimization of tensor-network states with*
1190 *the honeycomb-lattice corner transfer matrix*, *Phys. Rev. B* **107**, 054424 (2023),
1191 doi:[10.1103/PhysRevB.107.054424](https://doi.org/10.1103/PhysRevB.107.054424).
- 1192 [45] F. Wilde, A. Kshetrimayum, I. Roth, D. Hangleiter, R. Sweke and J. Eisert, *Scalably*
1193 *learning quantum many-body Hamiltonians from dynamical data* (2022), [https://arxiv.](https://arxiv.org/abs/2209.14328)
1194 [org/abs/2209.14328](https://arxiv.org/abs/2209.14328).
- 1195 [46] I. V. Lukin and A. G. Sotnikov, *Variational optimization of tensor-network states with*
1196 *the honeycomb-lattice corner transfer matrix*, *Phys. Rev. B* **107**, 054424 (2023),
1197 doi:[10.1103/PhysRevB.107.054424](https://doi.org/10.1103/PhysRevB.107.054424).

- 1198 [47] X.-Y. Zhang, S. Liang, H.-J. Liao, W. Li and L. Wang, *Differentiable program-*
1199 *ming tensor networks for kitaev magnets*, Phys. Rev. B **108**, 085103 (2023),
1200 doi:[10.1103/PhysRevB.108.085103](https://doi.org/10.1103/PhysRevB.108.085103).
- 1201 [48] F. Ferrari, S. Niu, J. Hasik, Y. Iqbal, D. Poilblanc and F. Becca, *Static and dynamical*
1202 *signatures of Dzyaloshinskii-Moriya interactions in the Heisenberg model on the kagome*
1203 *lattice*, SciPost Phys. **14**, 139 (2023), doi:[10.21468/SciPostPhys.14.6.139](https://doi.org/10.21468/SciPostPhys.14.6.139).
- 1204 [49] E. L. Weerda and M. Rizzi, *Fractional quantum hall states with variational projected*
1205 *entangled-pair states: a study of the bosonic harper-hofstadter model* (2023), [https://](https://arxiv.org/abs/2309.12811)
1206 arxiv.org/abs/2309.12811.
- 1207 [50] J. Hasik and G. B. Mbeng, *peps-torch: A differentiable tensor network library for two-*
1208 *dimensional lattice models*, GitHub, <https://github.com/jurajHasik/peps-torch>.
- 1209 [51] B. Ponsioen, *AD-PEPS*, GitHub, <https://github.com/b1592/ad-peps>.
- 1210 [52] J. Gray, *quimb: A python package for quantum information and many-body calculations*,
1211 *Journal of Open Source Software* **3**(29), 819, doi:[10.21105/joss.00819](https://doi.org/10.21105/joss.00819).
- 1212 [53] PEPSKit contributors, *PEPSKit: Tools for working with projected entangled-pair states.*,
1213 GitHub, <https://github.com/quantumghent/PEPSKit.jl>.
- 1214 [54] J. Dubail and N. Read, *Tensor network trial states for chiral topological phases in two*
1215 *dimensions and a no-go theorem in any dimension*, Phys. Rev. B **92**, 205307 (2015),
1216 doi:[10.1103/PhysRevB.92.205307](https://doi.org/10.1103/PhysRevB.92.205307).
- 1217 [55] Y. Xu, S. Capponi, J.-Y. Chen, L. Vanderstraeten, J. Hasik, A. H. Nevidomskyy, M. Mam-
1218 brini, K. Penc and D. Poilblanc, *Phase diagram of the chiral su(3) antiferromagnet on the*
1219 *kagome lattice*, Phys. Rev. B **108**, 195153 (2023), doi:[10.1103/PhysRevB.108.195153](https://doi.org/10.1103/PhysRevB.108.195153).
- 1220 [56] J. Naumann and E. L. Weerda, *variPEPS – a versatile tensor network library for varia-*
1221 *tional ground state simulations in two spatial dimensions*, GitHub, [https://github.com/](https://github.com/variPEPS)
1222 [variPEPS](https://github.com/variPEPS).
- 1223 [57] J. Naumann, P. Schmoll, F. Wilde and F. Krein, *variPEPS (Python version)*, Zenodo,
1224 doi:[10.5281/ZENODO.10852390](https://doi.org/10.5281/ZENODO.10852390).
- 1225 [58] E. L. Weerda, *VariPEPS.jl*, Zenodo, doi:[10.5281/zenodo.10974459](https://doi.org/10.5281/zenodo.10974459).
- 1226 [59] L. Vanderstraeten, L. Burgelman, B. Ponsioen, M. Van Damme, B. Vanhecke, P. Corboz,
1227 J. Haegeman and F. Verstraete, *Variational methods for contracting projected entangled-*
1228 *pair states*, Phys. Rev. B **105**, 195140 (2022), doi:[10.1103/PhysRevB.105.195140](https://doi.org/10.1103/PhysRevB.105.195140).
- 1229 [60] A. Nietner, B. Vanhecke, F. Verstraete, J. Eisert and L. Vanderstraeten, *Efficient varia-*
1230 *tional contraction of two-dimensional tensor networks with a non-trivial unit cell*, Quan-
1231 *tum* **4**, 328 (2020), doi:[10.22331/q-2020-09-21-328](https://doi.org/10.22331/q-2020-09-21-328).
- 1232 [61] J. Hasik and P. Corboz, *Incommensurate order with translationally invariant projected*
1233 *entangled-pair states: Spiral states and quantum spin liquid on the anisotropic triangular*
1234 *lattice* (2023), <https://arxiv.org/abs/2311.05534>.
- 1235 [62] P. Corboz, J. Jordan and G. Vidal, *Simulation of fermionic lattice models in two dimensions*
1236 *with projected entangled-pair states: Next-nearest neighbor hamiltonians*, Phys. Rev. B **82**,
1237 245119 (2010), doi:[10.1103/PhysRevB.82.245119](https://doi.org/10.1103/PhysRevB.82.245119).

- 1238 [63] P. Corboz, T. M. Rice and M. Troyer, *Competing states in the t - j model: Uni-*
1239 *form d -wave state versus stripe state*, Phys. Rev. Lett. **113**, 046402 (2014),
1240 doi:[10.1103/PhysRevLett.113.046402](https://doi.org/10.1103/PhysRevLett.113.046402).
- 1241 [64] M. T. Fishman, L. Vanderstraeten, V. Zauner-Stauber, J. Haegeman and F. Verstraete,
1242 *Faster methods for contracting infinite two-dimensional tensor networks*, Phys. Rev. B **98**,
1243 235148 (2018), doi:[10.1103/PhysRevB.98.235148](https://doi.org/10.1103/PhysRevB.98.235148).
- 1244 [65] W. Lan and G. Evenbly, *Reduced contraction costs of corner-transfer methods for PEPS*
1245 (2023), <https://arxiv.org/abs/2306.08212>.
- 1246 [66] A. Francuz, N. Schuch and B. Vanhecke, *Stable and efficient differentiation of tensor*
1247 *network algorithms* (2023), <https://arxiv.org/abs/2311.11894>.
- 1248 [67] J. Nocedal and S. J. Wright, *Calculating Derivatives*, pp. 193–219, Springer New York,
1249 New York, NY, ISBN 978-0-387-40065-5, doi:[10.1007/978-0-387-40065-5_8](https://doi.org/10.1007/978-0-387-40065-5_8) (2006).
- 1250 [68] M. Hestenes and E. Stiefel, *Methods of conjugate gradients for solving linear systems*, J.
1251 Res. Natl. Bur. Stand. **49**(6), 409 (1952), doi:[10.6028/jres.049.044](https://doi.org/10.6028/jres.049.044).
- 1252 [69] R. Fletcher, *Function minimization by conjugate gradients*, Comp. J. **7**(2), 149 (1964),
1253 doi:[10.1093/comjnl/7.2.149](https://doi.org/10.1093/comjnl/7.2.149).
- 1254 [70] Y. H. Dai and Y. Yuan, *A nonlinear conjugate gradient method with a strong global conver-*
1255 *gence property*, SIAM J. Opt. **10**(1), 177 (1999), doi:[10.1137/s1052623497318992](https://doi.org/10.1137/s1052623497318992).
- 1256 [71] E. Polak and G. Ribiere, *Note sur la convergence de méthodes de directions conjuguées*,
1257 Revue française d’informatique et de recherche opérationnelle. Série rouge **3**(16), 35
1258 (1969), doi:[10.1051/m2an/196903r100351](https://doi.org/10.1051/m2an/196903r100351).
- 1259 [72] W. W. Hager and H. Zhang, *A new conjugate gradient method with guaranteed descent*
1260 *and an efficient line search*, SIAM J. Opt. **16**(1), 170 (2005), doi:[10.1137/030601880](https://doi.org/10.1137/030601880).
- 1261 [73] H. Matthies and G. Strang, *The solution of nonlinear finite element equations*, Int. J.
1262 Num. Meth. Eng. **14**(11), 1613 (1979), doi:[10.1002/nme.1620141104](https://doi.org/10.1002/nme.1620141104).
- 1263 [74] J. Nocedal, *Updating quasi-newton matrices with limited storage*, Math. Comp. **35**(151),
1264 773 (1980), doi:[10.1090/s0025-5718-1980-0572855-7](https://doi.org/10.1090/s0025-5718-1980-0572855-7).
- 1265 [75] C. G. Broyden, *The convergence of a class of double-rank minimization algorithms 1. gen-*
1266 *eral considerations*, IMA J. Appl. Math. **6**(1), 76 (1970), doi:[10.1093/imamat/6.1.76](https://doi.org/10.1093/imamat/6.1.76).
- 1267 [76] R. Fletcher, *A new approach to variable metric algorithms*, Comp. J. **13**(3), 317 (1970),
1268 doi:[10.1093/comjnl/13.3.317](https://doi.org/10.1093/comjnl/13.3.317).
- 1269 [77] D. Goldfarb, *A family of variable-metric methods derived by variational means*, Math.
1270 Comp. **24**(109), 23 (1970), doi:[10.1090/s0025-5718-1970-0258249-6](https://doi.org/10.1090/s0025-5718-1970-0258249-6).
- 1271 [78] D. F. Shanno, *Conditioning of quasi-newton methods for function minimization*, Math.
1272 Comp. **24**(111), 647 (1970), doi:[10.1090/s0025-5718-1970-0274029-x](https://doi.org/10.1090/s0025-5718-1970-0274029-x).
- 1273 [79] J. Nocedal and S. J. Wright, *Fundamentals of Unconstrained Optimization*, pp. 10–29,
1274 Springer New York, New York, NY, ISBN 978-0-387-40065-5, doi:[10.1007/978-0-387-](https://doi.org/10.1007/978-0-387-40065-5_2)
1275 [40065-5_2](https://doi.org/10.1007/978-0-387-40065-5_2) (2006).
- 1276 [80] D. C. Liu and J. Nocedal, *On the limited memory bfgs method for large scale optimization*,
1277 Math. Prog. **45**(1-3), 503 (1989), doi:[10.1007/bf01589116](https://doi.org/10.1007/bf01589116).

- 1278 [81] L. Armijo, *Minimization of Functions Having Lipschitz Continuous First Partial Deriva-*
1279 *tives*, Pac. J. Math. **16**(1), 1 (1966), doi:[10.2140/pjm.1966.16.1](https://doi.org/10.2140/pjm.1966.16.1).
- 1280 [82] P. Wolfe, *Convergence conditions for ascent methods*, SIAM Rev. **11**(2), 226 (1969),
1281 doi:[10.1137/1011036](https://doi.org/10.1137/1011036).
- 1282 [83] P. Wolfe, *Convergence conditions for ascent methods. ii: Some corrections*, SIAM Rev.
1283 **13**(2), 185 (1971), doi:[10.1137/1013035](https://doi.org/10.1137/1013035).
- 1284 [84] J. Nocedal and S. J. Wright, *Line Search Methods*, pp. 30–65, Springer New York, New
1285 York, NY, ISBN 978-0-387-40065-5, doi:[10.1007/978-0-387-40065-5_3](https://doi.org/10.1007/978-0-387-40065-5_3) (2006).
- 1286 [85] S. Singh, R. N. C. Pfeifer and G. Vidal, *Tensor network decompositions in the presence of a*
1287 *global symmetry*, Phys. Rev. A **82**, 050301 (2010), doi:[10.1103/PhysRevA.82.050301](https://doi.org/10.1103/PhysRevA.82.050301).
- 1288 [86] P. Silvi, F. Tschirsich, M. Gerster, J. Jünemann, D. Jaschke, M. Rizzi and S. Montangero,
1289 *The Tensor Networks Anthology: Simulation techniques for many-body quantum lattice*
1290 *systems*, SciPost Phys. Lect. Notes p. 8 (2019), doi:[10.21468/SciPostPhysLectNotes.8](https://doi.org/10.21468/SciPostPhysLectNotes.8).
- 1291 [87] A. Weichselbaum, *Non-abelian symmetries in tensor networks: A quantum symmetry*
1292 *space approach*, Annals of Physics **327**(12), 2972 (2012).
- 1293 [88] P. Schmall, S. Singh, M. Rizzi and R. Orús, *A programming guide for ten-*
1294 *sor networks with global SU(2) symmetry*, Ann. Phys. **419**, 168232 (2020),
1295 doi:[10.1016/j.aop.2020.168232](https://doi.org/10.1016/j.aop.2020.168232).
- 1296 [89] B. Bruognolo, J.-W. Li, J. von Delft and A. Weichselbaum, *A beginner's guide to*
1297 *non-abelian iPEPS for correlated fermions*, SciPost Phys. Lect. Notes p. 25 (2021),
1298 doi:[10.21468/SciPostPhysLectNotes.25](https://doi.org/10.21468/SciPostPhysLectNotes.25).
- 1299 [90] Q. Mortier, L. Devos, L. Burgelman, B. Vanhecke, N. Bultinck, F. Verstraete, J. Haegeman
1300 and L. Vanderstraeten, *Fermionic tensor network methods* (2024), [2404.14611](https://arxiv.org/abs/2404.14611).
- 1301 [91] J. Haegeman, L. Devos, M. Hauru, H. Nakano, M. V. Damme, G. Roose, S. Carlström and
1302 X. Dong, *Jutho/TensorKit.jl: v0.12.2*, Zenodo, doi:[10.5281/zenodo.10574897](https://doi.org/10.5281/zenodo.10574897) (2024).
- 1303 [92] L. Devos, L. Burgelman, B. Vanhecke, J. Haegeman, F. Verstraete and L. Vanderstraeten,
1304 *TensorTrack*, doi:[10.5281/zenodo.6670354](https://doi.org/10.5281/zenodo.6670354) (2024).
- 1305 [93] A. Weichselbaum, *QSpace - An open-source tensor library for Abelian and non-Abelian*
1306 *symmetries* (2024), <https://arxiv.org/abs/2405.06632>.
- 1307 [94] C. Roberts, A. Milsted, M. Ganahl, A. Zalcman, B. Fontaine, Y. Zou, J. Hidary, G. Vidal
1308 and S. Leichenauer, *TensorNetwork: A Library for Physics and Machine Learning* (2019),
1309 <https://arxiv.org/abs/1905.01330>.
- 1310 [95] J. Haegeman, *KrylovKit*, Zenodo, doi:[10.5281/zenodo.10884302](https://doi.org/10.5281/zenodo.10884302) (2024).
- 1311 [96] IterativeSolvers contributors, *IterativeSolvers: A Julia package that provides iterative*
1312 *algorithms for solving linear systems, eigensystems, and singular value problems.*, GitHub,
1313 <https://github.com/JuliaLinearAlgebra/IterativeSolvers.jl>.
- 1314 [97] U. Schollwöck, *The density-matrix renormalization group in the age of matrix product*
1315 *states*, Annals of Physics **326**(1), 96 (2011).

- 1316 [98] H. C. Jiang, Z. Y. Weng and T. Xiang, *Accurate determination of tensor network state*
1317 *of quantum lattice models in two dimensions*, Phys. Rev. Lett. **101**, 090603 (2008),
1318 doi:[10.1103/PhysRevLett.101.090603](https://doi.org/10.1103/PhysRevLett.101.090603).
- 1319 [99] J. Liu, F. Wilde, A. A. Mele, L. Jiang and J. Eisert, *Stochastic noise can be helpful for*
1320 *variational quantum algorithms* (2023), <https://arxiv.org/abs/2210.06723>.
- 1321 [100] M. Rader and A. M. Läuchli, *Finite Correlation Length Scaling in Lorentz-*
1322 *Invariant Gapless iPEPS Wave Functions*, Phys. Rev. X **8**, 031030 (2018),
1323 doi:[10.1103/PhysRevX.8.031030](https://doi.org/10.1103/PhysRevX.8.031030).
- 1324 [101] P. Corboz, P. Czarnik, G. Kapteijns and L. Tagliacozzo, *Finite correlation length scal-*
1325 *ing with infinite projected entangled-pair states*, Phys. Rev. X **8**, 031031 (2018),
1326 doi:[10.1103/PhysRevX.8.031031](https://doi.org/10.1103/PhysRevX.8.031031).
- 1327 [102] P. Czarnik and P. Corboz, *Finite correlation length scaling with infinite projected*
1328 *entangled pair states at finite temperature*, Phys. Rev. B **99**, 245107 (2019),
1329 doi:[10.1103/PhysRevB.99.245107](https://doi.org/10.1103/PhysRevB.99.245107).
- 1330 [103] B. Vanhecke, J. Hasik, F. Verstraete and L. Vanderstraeten, *Scaling hypothe-*
1331 *sis for projected entangled-pair states*, Phys. Rev. Lett. **129**, 200601 (2022),
1332 doi:[10.1103/PhysRevLett.129.200601](https://doi.org/10.1103/PhysRevLett.129.200601).
- 1333 [104] B. Ponsioen, J. Hasik and P. Corboz, *Improved summations of n-point correlation functions*
1334 *of projected entangled-pair states* (2023), <https://arxiv.org/abs/2306.13327>.
- 1335 [105] S. Nyckees, A. Rufino, F. Mila and J. Colbois, *Critical line of the triangular ising antifer-*
1336 *romagnet in a field from a C_3 -symmetric corner transfer matrix algorithm*, Phys. Rev. E
1337 **108**, 064132 (2023), doi:[10.1103/PhysRevE.108.064132](https://doi.org/10.1103/PhysRevE.108.064132).
- 1338 [106] I. V. Lukin and A. G. Sotnikov, *Corner transfer matrix renormalization group approach in*
1339 *the zoo of archimedean lattices* (2024), <https://arxiv.org/abs/2401.07274>.
- 1340 [107] A. Kitaev, *Anyons in an exactly solved model and beyond*, Ann. Phys. **321**(1), 2 (2006),
1341 doi:[10.1016/j.aop.2005.10.005](https://doi.org/10.1016/j.aop.2005.10.005).
- 1342 [108] Z. Y. Xie, J. Chen, J. F. Yu, X. Kong, B. Normand and T. Xiang, *Tensor renormalization*
1343 *of quantum many-body systems using projected entangled simplex states*, Phys. Rev. X **4**,
1344 011025 (2014), doi:[10.1103/PhysRevX.4.011025](https://doi.org/10.1103/PhysRevX.4.011025).
- 1345 [109] P. Schmoll, S. S. Jahromi, M. Hörmann, M. Mühlhauser, K. P. Schmidt and R. Orús,
1346 *Fine grained tensor network methods*, Phys. Rev. Lett. **124**, 200603 (2020),
1347 doi:[10.1103/PhysRevLett.124.200603](https://doi.org/10.1103/PhysRevLett.124.200603).
- 1348 [110] P. W. Anderson, *Limits on the energy of the antiferromagnetic ground state*, Phys. Rev.
1349 **83**, 1260 (1951), doi:[10.1103/PhysRev.83.1260](https://doi.org/10.1103/PhysRev.83.1260).
- 1350 [111] I. V. Lukin and A. G. Sotnikov, *Variational optimization of tensor-network states with*
1351 *the honeycomb-lattice corner transfer matrix*, Phys. Rev. B **107**(5), 054424 (2023),
1352 doi:[10.1103/physrevb.107.054424](https://doi.org/10.1103/physrevb.107.054424).
- 1353 [112] D. J. J. Farnell, O. Götze, J. Richter, R. F. Bishop and P. H. Y. Li, *Quantum*
1354 *spin- $\frac{1}{2}$ antiferromagnets on Archimedean lattices: The route from semiclassical mag-*
1355 *netic order to nonmagnetic quantum states*, Phys. Rev. B **89**(18), 184407 (2014),
1356 doi:[10.1103/physrevb.89.184407](https://doi.org/10.1103/physrevb.89.184407).

- 1357 [113] F. J. Jiang, *High precision determination of the low-energy constants for the two-*
1358 *dimensional quantum heisenberg model on the honeycomb lattice*, *Europ. Phys. J. B*
1359 **85**(12), 402 (2012), doi:[10.1140/epjb/e2012-30784-7](https://doi.org/10.1140/epjb/e2012-30784-7).
- 1360 [114] R. Ganesh, J. van den Brink and S. Nishimoto, *Deconfined criticality in the frus-*
1361 *trated heisenberg honeycomb antiferromagnet*, *Phys. Rev. Lett.* **110**, 127203 (2013),
1362 doi:[10.1103/PhysRevLett.110.127203](https://doi.org/10.1103/PhysRevLett.110.127203).
- 1363 [115] S.-S. Gong, D. N. Sheng, O. I. Motrunich and M. P. A. Fisher, *Phase diagram of the*
1364 *spin- $\frac{1}{2}$ J_1 - J_2 Heisenberg model on a honeycomb lattice*, *Phys. Rev. B* **88**, 165138 (2013),
1365 doi:[10.1103/PhysRevB.88.165138](https://doi.org/10.1103/PhysRevB.88.165138).
- 1366 [116] H. J. Liao, Z. Y. Xie, J. Chen, Z. Y. Liu, H. D. Xie, R. Z. Huang, B. Normand and T. Xiang,
1367 *Gapless spin-liquid ground state in the $s = 1/2$ kagome antiferromagnet*, *Phys. Rev. Lett.*
1368 **118**, 137202 (2017), doi:[10.1103/PhysRevLett.118.137202](https://doi.org/10.1103/PhysRevLett.118.137202).
- 1369 [117] A. M. Läuchli, J. Sudan and R. Moessner, *Spin- $\frac{1}{2}$ kagome Heisenberg antiferromagnet*
1370 *revisited*, *Phys. Rev. B* **100**(15), 155142 (2019), doi:[10.1103/physrevb.100.155142](https://doi.org/10.1103/physrevb.100.155142).
- 1371 [118] S. Yan, D. A. Huse and S. R. White, *Spin-Liquid Ground State of the S*
1372 *$= 1/2$ Kagome Heisenberg Antiferromagnet*, *Science* **332**(6034), 1173 (2011),
1373 doi:[10.1126/science.1201080](https://doi.org/10.1126/science.1201080).
- 1374 [119] S. Depenbrock, I. P. McCulloch and U. Schollwöck, *Nature of the spin-liquid ground state*
1375 *of the $s = 1/2$ heisenberg model on the kagome lattice*, *Phys. Rev. Lett.* **109**, 067201
1376 (2012), doi:[10.1103/PhysRevLett.109.067201](https://doi.org/10.1103/PhysRevLett.109.067201).
- 1377 [120] Y.-C. He, M. P. Zaletel, M. Oshikawa and F. Pollmann, *Signatures of Dirac Cones in*
1378 *a DMRG Study of the Kagome Heisenberg Model*, *Phys. Rev. X* **7**, 031020 (2017),
1379 doi:[10.1103/PhysRevX.7.031020](https://doi.org/10.1103/PhysRevX.7.031020).
- 1380 [121] N. Astrakhantsev, F. Ferrari, N. Niggemann, T. Müller, A. Chauhan, A. Kshetrimayum,
1381 P. Ghosh, N. Regnault, R. Thomale, J. Reuther, T. Neupert and Y. Iqbal, *Pinwheel valence*
1382 *bond crystal ground state of the spin- $\frac{1}{2}$ heisenberg antiferromagnet on the shuriken lattice*,
1383 *Phys. Rev. B* **104**, L220408 (2021), doi:[10.1103/PhysRevB.104.L220408](https://doi.org/10.1103/PhysRevB.104.L220408).
- 1384 [122] P. Schmoll, A. Kshetrimayum, J. Naumann, J. Eisert and Y. Iqbal, *Tensor network study of*
1385 *the spin- $\frac{1}{2}$ Heisenberg antiferromagnet on the shuriken lattice*, *Phys. Rev. B* **107**, 064406
1386 (2023), doi:[10.1103/PhysRevB.107.064406](https://doi.org/10.1103/PhysRevB.107.064406).
- 1387 [123] M. Fujihala, K. Morita, R. Mole, S. Mitsuda, T. Tohyama, S.-I. Yano, D. Yu, S. Sota,
1388 T. Kuwai, A. Koda, H. Okabe, H. Lee *et al.*, *Gapless spin liquid in a square-kagome lattice*
1389 *antiferromagnet*, *Nature Comm.* **11**, 3429 (2020), doi:[10.1038/s41467-020-17235-z](https://doi.org/10.1038/s41467-020-17235-z).
- 1390 [124] Q. Li, H. Li, J. Zhao, H.-G. Luo and Z. Y. Xie, *Magnetization of the spin- $\frac{1}{2}$ heisen-*
1391 *berg antiferromagnet on the triangular lattice*, *Phys. Rev. B* **105**, 184418 (2022),
1392 doi:[10.1103/PhysRevB.105.184418](https://doi.org/10.1103/PhysRevB.105.184418).
- 1393 [125] D. A. Huse and V. Elser, *Simple variational wave functions for two-dimensional*
1394 *heisenberg spin- $\frac{1}{2}$ antiferromagnets*, *Phys. Rev. Lett.* **60**, 2531 (1988),
1395 doi:[10.1103/PhysRevLett.60.2531](https://doi.org/10.1103/PhysRevLett.60.2531).
- 1396 [126] S. R. White and A. L. Chernyshev, *Neél order in square and triangular lattice heisenberg*
1397 *models*, *Phys. Rev. Lett.* **99**, 127004 (2007), doi:[10.1103/PhysRevLett.99.127004](https://doi.org/10.1103/PhysRevLett.99.127004).

- 1398 [127] S. Yunoki and S. Sorella, *Two spin liquid phases in the spatially anisotropic triangular*
1399 *heisenberg model*, Phys. Rev. B **74**, 014408 (2006), doi:[10.1103/PhysRevB.74.014408](https://doi.org/10.1103/PhysRevB.74.014408).
- 1400 [128] V. Zauner, D. Draxler, L. Vanderstraeten, M. Degroote, J. Haegeman, M. M. Rams, V. Sto-
1401 jevic, N. Schuch and F. Verstraete, *Transfer matrices and excitations with matrix product*
1402 *states*, New J. Phys. **17**, 053002 (2015), doi:[10.1088/1367-2630/17/5/053002](https://doi.org/10.1088/1367-2630/17/5/053002).
- 1403 [129] L. Vanderstraeten, M. Mariën, F. Verstraete and J. Haegeman, *Excitations and the*
1404 *tangent space of projected entangled-pair states*, Phys. Rev. B **92**, 201111 (2015),
1405 doi:[10.1103/PhysRevB.92.201111](https://doi.org/10.1103/PhysRevB.92.201111).
- 1406 [130] L. Vanderstraeten, J. Haegeman and F. Verstraete, *Simulating excitation spec-*
1407 *tra with projected entangled-pair states*, Phys. Rev. B **99**, 165121 (2019),
1408 doi:[10.1103/PhysRevB.99.165121](https://doi.org/10.1103/PhysRevB.99.165121).
- 1409 [131] B. Ponsioen and P. Corboz, *Excitations with projected entangled pair states us-*
1410 *ing the corner transfer matrix method*, Phys. Rev. B **101**, 195109 (2020),
1411 doi:[10.1103/PhysRevB.101.195109](https://doi.org/10.1103/PhysRevB.101.195109).
- 1412 [132] W.-L. Tu, L. Vanderstraeten, N. Schuch, H.-Y. Lee, N. Kawashima and J.-Y. Chen, *Gen-*
1413 *erating function for projected entangled-pair states* (2023), [https://arxiv.org/abs/2307.](https://arxiv.org/abs/2307.08083)
1414 [08083](https://arxiv.org/abs/2307.08083).
- 1415 [133] T. Barthel, C. Pineda and J. Eisert, *Contraction of fermionic operator circuits and*
1416 *the simulation of strongly correlated fermions*, Phys. Rev. A **80**, 042333 (2009),
1417 doi:[10.1103/PhysRevA.80.042333](https://doi.org/10.1103/PhysRevA.80.042333).
- 1418 [134] P. Corboz, G. Evenbly, F. Verstraete and G. Vidal, *Simulation of interacting*
1419 *fermions with entanglement renormalization*, Phys. Rev. A **81**, 010303 (2010),
1420 doi:[10.1103/PhysRevA.81.010303](https://doi.org/10.1103/PhysRevA.81.010303).
- 1421 [135] C. Wille, O. Buerschaper and J. Eisert, *Fermionic topological quantum states as tensor*
1422 *networks*, Phys. Rev. B **95**, 245127 (2017), doi:[10.1103/PhysRevB.95.245127](https://doi.org/10.1103/PhysRevB.95.245127).
- 1423 [136] N. Bultinck, D. J. Williamson, J. Haegeman and F. Verstraete, *Fermionic pro-*
1424 *jected entangled-pair states and topological phases*, J. Phys. A **51**, 025202 (2017),
1425 doi:[10.1088/1751-8121/aa99cc](https://doi.org/10.1088/1751-8121/aa99cc).
- 1426 [137] P. Corboz, R. Orús, B. Bauer and G. Vidal, *Simulation of strongly correlated fermions in*
1427 *two spatial dimensions with fermionic projected entangled-pair states*, Phys. Rev. B **81**,
1428 165104 (2010), doi:[10.1103/PhysRevB.81.165104](https://doi.org/10.1103/PhysRevB.81.165104).
- 1429 [138] I. Pižorn and F. Verstraete, *Fermionic implementation of projected entangled pair states*
1430 *algorithm*, Phys. Rev. B **81**, 245110 (2010), doi:[10.1103/PhysRevB.81.245110](https://doi.org/10.1103/PhysRevB.81.245110).
- 1431 [139] R. Sweke, P. Boes, N. Ng, C. Sparaciari, J. Eisert and M. Goihl, *Transparent Reporting*
1432 *of Research-Related Greenhouse Gas Emissions Through the Scientific CO₂nduct Initiative*,
1433 Comm. Phys. **5**(1), 150 (2022), doi:[10.1038/s42005-022-00930-2](https://doi.org/10.1038/s42005-022-00930-2).
- 1434 [140] J. Bradbury, R. Frostig, P. Hawkins, M. J. Johnson, C. Leary, D. Maclaurin, G. Necula,
1435 A. Paszke, J. VanderPlas, S. Wanderman-Milne and Q. Zhang, *JAX: composable trans-*
1436 *formations of Python+NumPy programs*, GitHub, <http://github.com/google/jax>.
- 1437 [141] R. Frostig, M. Johnson and C. Leary, *Compiling machine learning programs via high-level*
1438 *tracing* (2018), <https://mlsys.org/Conferences/2019/doc/2018/146.pdf>.

- 1439 [142] Quantum Group UGent, *Open-source software and notebooks*, <https://quantumghent.github.io/software/>.
1440
- 1441 [143] Zygote contributors, *Zygote: Source-to-source automatic differentiation (AD) in Julia, and the next-gen AD system for the Flux differentiable programming framework.*, GitHub,
1442 <https://github.com/FluxML/Zygote.jl>.
1443
- 1444 [144] J. S. Centre, *Jureca: Data centric and booster modules implementing the modular super-*
1445 *computing architecture at jülich supercomputing centre*, J. Large-Scale Res. Fac. **7**, A182
1446 (2021), doi:[10.17815/jlsrf-7-182](https://doi.org/10.17815/jlsrf-7-182).
- 1447 [145] M. B. Giles, *An extended collection of matrix derivative results for forward and reverse*
1448 *mode algorithmic differentiation* (2008), <https://people.maths.ox.ac.uk/gilesm/files/NA-08-01.pdf>.
1449
- 1450 [146] H. Xie, J.-G. Liu and L. Wang, *Automatic differentiation of dominant eigen-*
1451 *solver and its applications in quantum physics*, Phys. Rev. B **101**, 245139 (2020),
1452 doi:[10.1103/physrevb.101.245139](https://doi.org/10.1103/physrevb.101.245139).
- 1453 [147] Z.-Q. Wan and S.-X. Zhang, *Automatic differentiation for complex valued SVD* (2019),
1454 <https://arxiv.org/abs/1909.02659>.
- 1455 [148] B. Christianson, *Reverse accumulation and attractive fixed points*, Opt. Meth. Soft. **3**(4),
1456 311 (1994), doi:[10.1080/10556789408805572](https://doi.org/10.1080/10556789408805572).
- 1457 [149] Z. Kolter, D. Duvenaud and M. Johnson, *Deep implicit layers - Neural ODEs, deep*
1458 *equilibrium models, and beyond* (2020), [http://implicit-layers-tutorial.org/implicit_](http://implicit-layers-tutorial.org/implicit_functions/)
1459 [functions/](http://implicit-layers-tutorial.org/implicit_functions/).
- 1460 [150] M. J. Johnson and The JAX Authors, *Custom derivative rules for JAX-transformable*
1461 *Python functions* (2020), [https://jax.readthedocs.io/en/latest/notebooks/Custom_](https://jax.readthedocs.io/en/latest/notebooks/Custom_derivative_rules_for_Python_code.html)
1462 [derivative_rules_for_Python_code.html](https://jax.readthedocs.io/en/latest/notebooks/Custom_derivative_rules_for_Python_code.html).